

Banner appropriate to article type will appear here in typeset article

Dynamics of an oscillatory boundary layer over a sediment bed

Jonathan S. Van Doren¹ and M. Housse Kasaoui^{1†}

¹School for Engineering of Matter, Transport and Energy, Arizona State University, Tempe, AZ 85281, USA.

(Received xx; revised xx; accepted xx)

We investigate the dynamics of an oscillatory boundary layer developing over a bed of collisional and freely evolving sediment grains. We perform Euler-Lagrange simulations at Reynolds numbers $Re_\delta = 200, 400$, and 800 , density ratio $\rho_p/\rho_f = 2.65$, Galileo number $Ga = 51.9$, maximum Shields numbers from 2.79×10^{-2} to 4.40×10^{-2} , and Keulegan-Carpenter number from 134.5 to 538.0 . We show that the dynamics of the oscillatory boundary layer and sediment bed are strongly coupled due to two mechanisms: (I) bed permeability, which leads to flow penetration deep inside the sediment layer, a slip velocity at the bed-fluid interface, and the expansion of the boundary layer, and (II) particle motion, which leads to rolling-grain ripples at $Re_\delta = 400$ and sheet flow at $Re_\delta = 800$. While at $Re_\delta = 200$ the sediment bed remains static during the entire cycle, the permeability of the bed-fluid interface causes a thickening of the boundary layer and reduction of the bed shear stress by 38%. With increasing Re_δ , the particles become mobile, which leads to rolling-grain ripples at $Re_\delta = 400$ and suspended sediment at $Re_\delta = 800$. Due to their feedback force on the fluid, the mobile sediment particles cause greater velocity fluctuations in the fluid. In addition, greater flow intrusion causes the bed shear stress to decrease by 54% at $Re_\delta = 400$ and 79% at $Re_\delta = 800$, compared to the flow over a smooth and impermeable wall.

Key words: keyword 1, keyword 2, keyword 3

MSC Codes (*Optional*) Please enter your MSC Codes here

1. Introduction

In shallow areas of the ocean, the seafloor may be subject to large oscillating pressure gradients and strong shear forces. This causes sediment to become suspended and transported to new locations, where they are deposited as the shear force oscillates. A model flow often used to investigate this process is the oscillatory

† Email address for correspondence: houssem.kasaoui@asu.edu

boundary layer (OBL) problem. Stokes (1855) was amongst the first to address this problem, specifically in the limit where viscous effects dominate and where the bottom surface is represented as a smooth flat wall. Under these assumptions, Stokes (1855) derived analytical solutions which show the establishment of a boundary layer with characteristic thickness $\delta = \sqrt{2\nu/\omega}$, where ν is the fluid kinematic viscosity and ω the angular frequency of the oscillations. Due to the assumption of dominating viscous effects, these solutions apply only in the limit of very small Reynolds numbers $Re_\delta = U_0\delta/\nu$, where U_0 is the velocity amplitude of the oscillations. Later, many researchers investigated the dynamics of oscillatory boundary layers over smooth and rough walls at larger Reynolds numbers, including when the Reynolds number is sufficiently high for turbulence to emerge (Akhavan *et al.* 1991b; Carstensen *et al.* 2010, 2012; Costamagna *et al.* 2003; Fytanidis *et al.* 2021; Ghodke & Apte 2016, 2018; Hino *et al.* 1976; Mazzuoli & Vittori 2019; Mazzuoli *et al.* 2020, 2016; Ozdemir *et al.* 2014; Pedocchi *et al.* 2011; Salon *et al.* 2007; Sarpkaya 1993; Vittori & Verzicco 1998; Vittori *et al.* 2020). However, it is unclear whether these results are applicable to seafloors. Unlike the previously studied configurations with impermeable and fixed smooth or rough walls, seafloors are made of sediment particles that together form a porous bed. Depending on the details of the flow over it, the bed may be static, with or without bedforms, and may even evolve dynamically as sediment particles saltate or become suspended by the flow (Finn *et al.* 2016). In this manuscript, we investigate how the dynamics of an OBL couple with those of a bottom collisional and freely evolving sediment bed at increasingly large Reynolds numbers.

There has been significant effort devoted to the characterization of the boundary layer that develops over a smooth or rough wall under the action of an oscillatory forcing. Depending on the Reynolds number Re_δ , different regimes have been identified, as detailed in (Vittori & Verzicco 1998; Pedocchi *et al.* 2011; Akhavan *et al.* 1991a; Ozdemir *et al.* 2014; Fytanidis *et al.* 2021). To summarize, an OBL developing over an impermeable wall may exhibit four different regimes. The laminar regime occurs in smooth, rough, and wavy wall OBL at $Re_\delta \lesssim 85$. In this regime, the flow is laminar throughout the oscillation cycle (Blondeaux & Seminara 1979; Vittori & Verzicco 1998; Akhavan *et al.* 1991a), and is well described by the analytical solutions of Stokes (1855). For $85 \lesssim Re_\delta \lesssim 550$, the flow is in the disturbed laminar regime (Hino *et al.* 1976; Jensen *et al.* 1989). The latter is characterized by the appearance of small amplitude perturbations superimposed upon the Stokes flow (Vittori & Verzicco 1998). Fytanidis *et al.* (2021) found that the Reynolds number thresholds for this regime depend strongly on background disturbances. For $550 \lesssim Re_\delta \lesssim 3460$, the flow enters the intermittent turbulent regime and is characterized by sudden turbulence eruption during the decelerating portion of the oscillatory period before relaminarizing again. Lastly, the turbulent regime occurs for $Re_\delta \gtrsim 3460$. In this regime, Jensen *et al.* (1989) show that the OBL presents sustained velocity fluctuations and a logarithmic layer for at least 90 percent of the cycle.

Note that, with a bottom rough wall, the Reynolds number thresholds between the different regimes may vary considerably, as the flow characteristics depend on additional roughness parameters, such as the Keulegan-Carpenter number $KC = U_0/(\omega d_p)$, where d_p represents the roughness size. Jensen *et al.* (1989) showed that disturbances caused by fixed sandpaper roughness leads to a thicker boundary layer and increased turbulence. Similarly, Xiong *et al.* (2020) found that a flow disturbance created by a wall mounted obstacle leads to earlier transition to turbulence, thereby

lowering the threshold Re_δ compared to the one found for a smooth wall OBL. Additional studies of roughness effects can be found in (Ghodke & Apte 2016, 2018; Mazzuoli & Vittori 2019).

Permeability may also have a significant effect on the structure of an OBL developing over a particle bed. Conley & Inman (1994) performed experiments with a ventilated OBL, that is, an oscillatory boundary layer with periodic transpiration over a permeable wall. They found that the wall shear stress decreases during suction and increases during injection. For a permeable wall, the no-slip condition may no longer hold, as observed by Liu *et al.* (1996) and Breugem *et al.* (2006). By comparing simulations of an OBL with experimental data, Meza-Valle & Pujara (2022) showed that a mixed boundary condition at the surface best captures the flow over a permeable wall. A permeable bed allows flow penetration, which in turn creates a Kelvin-Helmholtz instability and an inflection point in the fluid velocity within the boundary layer (Sparrow *et al.* 2012; Voermans *et al.* 2017). All these modifications caused by the bed permeability make it difficult to estimate the bed shear stress beforehand (Yuan & Madsen 2014).

The studies discussed thus far considered fixed porous beds. In the case of mobile beds, particle transport may further alter the bed fluid interface. Particle motion leads to the emergence of new regimes, as discussed by Finn & Li (2016), who proposed a regime map for sediment-turbulent interactions. In the no-motion regime, the bed remains stationary and acts as previously described. In the bedform regime, ripples emerge in the particle bed as particles saltate over the surface. The study of Mazzuoli *et al.* (2019), by means of particle-resolved direct numerical simulations (PR-DNS), illustrates this regime. The authors showed the emergence of rolling-grain ripples in an OBL developing over a sediment bed at $Re_\delta \sim 100$, density ratio $\rho_p/\rho_f \sim 2.5$, and Galileo number $Ga \sim 10$. The latter represents the relative effect of gravitational and viscous forces exerted on sediment grains. An earlier study showed that ripples emerge from the interaction between particle rows and recirculation zones in the OBL (Mazzuoli *et al.* 2016). In the sheet flow regime, the bed-fluid interface recedes due to the formation of a layer of suspended particles (Hsu *et al.* 2004; O'Donoghue & Wright 2004). Mazzuoli *et al.* (2020) showed that the eruption of turbulence plays a role in the sediment resuspension. Further, at relatively low values of Shields number, sediment transport may depend on both Shields number and flow acceleration.

Several computational methods can be leveraged to study the dynamics of an oscillatory boundary layer over a sediment bed. Particle-Resolved Direct Numerical Simulation (PR-DNS), in which the boundary layer around each sediment grain is fully resolved, provides the highest fidelity since it requires little to no-modeling (Uhlmann 2005; Apte *et al.* 2009; Kempe & Fröhlich 2012; Breugem 2012; Kasbaoui & Herrmann 2024). However, this results in very high computational cost, as seen from the PR-DNS of Mazzuoli *et al.* (2019). While using smaller computational domains and shorter integration times may reduce computational cost, it also introduces numerical artifacts. For example, the domain considered in the PR-DNS of Mazzuoli *et al.* (2020) was too small to allow the natural formation of ripples in the sediment bed. Even with this restrictive domain size, the high cost of the PR-DNS of Mazzuoli *et al.* (2020) limited the integration time to the first 1 to 4 cycles of the OBL, which may not be enough to reach a statistically periodic state. In contrast, the Euler-Lagrange method provide a good balance between computational cost and fidelity (Capecelatro & Desjardins 2013a; Finn *et al.* 2016). In this approach, flow features and bed dynamics on scales larger than the particle size are well resolved, while

the flow on the scale of the particle is modeled. This makes it possible to simulate the dynamics on length and time scales much larger than those accessible in PR-DNS. Earlier studies showed that this approach can reproduce with high fidelity the dynamics of dense fluidized beds Capecelatro & Desjardins (2013a) and dense slurries Capecelatro & Desjardins (2013b); Arolla & Desjardins (2015), including in sheet flow and bedform regimes. More recently, (Rao & Capecelatro 2019) showed that predictions with the Euler-Lagrange method for the evolution of sediment bed under both laminar and turbulent shear flow match very well with PR-DNS (Kidanemariam & Uhlmann 2014) and experiments (Aussillous *et al.* 2013).

In this paper, we study the interplay between an oscillatory boundary layer and a sediment bed made of collisional and freely evolving particles from the laminar regime to the onset of turbulence using Euler-Lagrange simulations. The structure of the manuscript is as follows. In section 2, we provide the governing equations that dictate the evolution of the flow and sediment particles. In section 3, we provide details on the computations and parameters used in this study. Next, we analyze statistics of the fluid and solid phases in section 4, highlighting how sediment bed dynamics couple with those of the oscillatory boundary layer. Finally, we give concluding remarks in section 5.

2. Governing equations

We use the volume-filtering approach of Anderson & Jackson (1967) and Euler-Lagrange methodology of Capecelatro & Desjardins (2013a) to describe the dynamics of the sediment-laden flow. The carrier phase is an incompressible fluid with density ρ_f and viscosity μ_f . The volume-filtered Navier-Stokes equations read

$$\frac{\partial}{\partial t}(\alpha_f \rho_f) + \nabla \cdot (\alpha_f \rho_f \mathbf{u}_f) = 0, \quad (2.1)$$

$$\frac{\partial}{\partial t}(\alpha_f \rho_f \mathbf{u}_f) + \nabla \cdot (\alpha_f \rho_f \mathbf{u}_f \mathbf{u}_f) = \nabla \cdot (\boldsymbol{\tau} + \mathbf{R}_\mu) + \alpha_f \rho_f \mathbf{g} - \mathbf{F}_p + \mathbf{A}, \quad (2.2)$$

where α_f is the fluid volume fraction, \mathbf{u}_f is the volume-filtered fluid velocity, $\boldsymbol{\tau} = -p\mathbf{I} + \mu[\nabla \mathbf{u}_f + \nabla \mathbf{u}_f^T - \frac{2}{3}(\nabla \cdot \mathbf{u}_f)\mathbf{I}]$ is the resolved fluid stress tensor (Capecelatro & Desjardins 2013a), p is pressure, which includes the hydrostatic contribution, \mathbf{g} is the gravitational acceleration, and \mathbf{F}_p is the momentum exchange between the particles and the fluid. The tensor \mathbf{R}_μ represents the so-called residual viscous stress tensor. This term arises from filtering the point-wise stress tensor. It includes sub-filter scale terms which require closure. This term is believed to be responsible for the apparent enhanced viscosity observed in viscous fluids containing suspended solid particles. For this reason, Capecelatro & Desjardins (2013a) proposed a closure using an effective viscosity, which when combined with the effective viscosity model of Gibilaro *et al.* (2007) leads to an expression for the residual viscous stress tensor

$$\mathbf{R}_\mu = \mu_f(\alpha_f^{-2.8} - 1)[\nabla \mathbf{u}_f + \nabla \mathbf{u}_f^T - \frac{2}{3}(\nabla \cdot \mathbf{u}_f)\mathbf{I}]. \quad (2.3)$$

In order to study the dynamics of an oscillatory boundary layer, we drive the flow using the last term in equation (2.2), which expresses as

$$\mathbf{A} = \alpha_f \rho_f U_0 \omega \cos(\omega t) \mathbf{e}_x. \quad (2.4)$$

This represents a harmonic pressure gradient forcing with angular frequency ω and velocity amplitude U_0 . Here, x is the coordinate in the streamwise direction along the

unitary vector \mathbf{e}_x , y is the coordinate in the wall normal direction, z is the coordinate in the spanwise direction.

The particles are described in the Lagrangian frame. Following Maxey & Riley (1983), the equations of motion of a particle “ i ” are given by

$$\frac{d\mathbf{x}_p^i}{dt}(t) = \mathbf{u}_p^i(t), \quad (2.5)$$

$$m_p \frac{d\mathbf{u}_p^i}{dt}(t) = \mathbf{f}_p^{h,i} + \mathbf{f}_p^{c,i}, \quad (2.6)$$

$$I_p \frac{d\boldsymbol{\omega}_p^i}{dt}(t) = \mathbf{T}_p^{c,i} \quad (2.7)$$

where \mathbf{x}_p^i , \mathbf{u}_p^i , $\boldsymbol{\omega}_p^i$, m_p , and I_p are the particle position, velocity, angular velocity, mass, and moment of inertia, respectively. $\mathbf{f}_p^{h,i}$ represents the hydrodynamic force, which is modeled as (Van Doren & Kasbaoui 2024)

$$\mathbf{f}_p^{h,i}(t) = V_p \nabla \cdot \boldsymbol{\tau}|_{\mathbf{x}_p^i} + m_p f_d \frac{\mathbf{u}_f(\mathbf{x}_p^i, t) - \mathbf{u}_p^i}{\tau_p} + \mathbf{f}_p^{\text{am},i} + \mathbf{f}_p^{\text{lift},i}. \quad (2.8)$$

where $V_p = \pi d_p^3/6$ is the particle volume. The first term on the right hand side of equation (2.8) represents the effect of the undisturbed flow field (Maxey & Riley 1983). The second term represents the drag force exerted on a particle. Note that, $\tau_p = \rho_p d_p^2/(18\mu)$ is the particle response time and f_d is a drag correction factor. We use the one by Tenneti *et al.* (2011), derived from particle-resolved direct numerical simulations, which accounts for both inertial and high particle volume fraction effects. The last two terms on the right hand side of (2.8) represent the added mass and Saffman lift Saffman (1965) forces,

$$\mathbf{f}_p^{\text{am},i} = \frac{1}{2} \alpha_f \rho_f V_p \left(\frac{d\mathbf{u}_p^i}{dt} - \frac{D\mathbf{u}_f(\mathbf{x}_p^i, t)}{Dt} \right) \quad (2.9)$$

$$\mathbf{f}_p^{\text{lift},i} = 1.615 J \mu_f d_p |\mathbf{u}_s^i| \sqrt{\frac{d_p^2 |\boldsymbol{\omega}^i| \rho_f \alpha_f}{\mu_f}} \frac{\boldsymbol{\omega}^i \times \mathbf{u}_s^i}{|\boldsymbol{\omega}^i| |\mathbf{u}_s^i|} \quad (2.10)$$

where $\boldsymbol{\omega}^i = \boldsymbol{\omega}_f(\mathbf{x}_p^i, t)$ is the fluid vorticity at the particle location, $\mathbf{u}_s^i = \mathbf{u}_f(\mathbf{x}_p^i, t) - \mathbf{u}_p^i$ is the slip velocity, J is a lift correction, which is equal to one in the model from Saffman (1965).

The term $\mathbf{f}_p^{c,i}$ represents the collisional force exerted on the particle due to particle-particle and particle-wall collisions. These collision are modeled using the soft sphere model, as detailed in (Capecelatro & Desjardins 2013a). Briefly, the force exerted on particle a due to a collision with particle b , denoted $\mathbf{f}_p^{c,b \rightarrow a}$, is decomposed into normal and tangential components. The normal component $\mathbf{f}_{p,n}^{c,b \rightarrow a}$ is modeled as a linearized spring-dashpot system, i.e,

$$\mathbf{f}_{p,n}^{c,b \rightarrow a} = \begin{cases} -k\delta_{ab} \mathbf{n}_{ab} - \eta \mathbf{u}_{ab,n} & \text{if } |\mathbf{x}_p^a - \mathbf{x}_p^b| < 0.5(d_p^a + d_p^b) + \lambda \\ 0 & \text{else.} \end{cases} \quad (2.11)$$

where $\delta_{ab} = 0.5(d_p^a + d_p^b) - |\mathbf{x}_p^a - \mathbf{x}_p^b|$ is the overlap between particles a and b , \mathbf{n}_{ab} is the unit normal vector between the particles, and $\mathbf{u}_{ab,n}$ is the normal relative velocity. The parameters k and the η are the spring stiffness and dampening factor, respectively. They are related to the reduced mass $m_{ab} = (1/m_a + 1/m_b)^{-1}$, collision

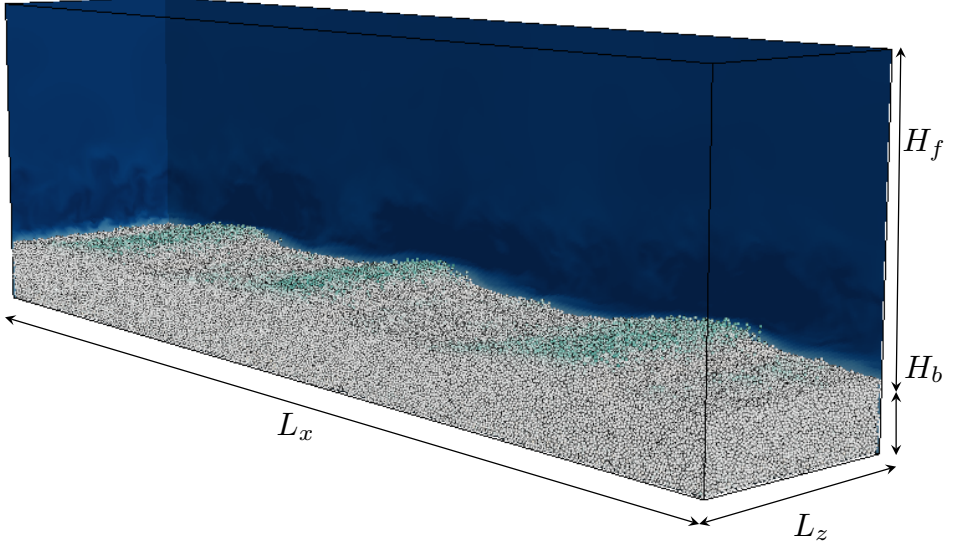


Figure 1: Schematic of the configuration with a bottom sediment bed. The latter is generated in precursor runs where the particles are seeded towards the middle of the domain and allowed to settle on the bottom boundary.

time τ_{col} , and coefficient of restitution e , as

$$k = \frac{m_{ab}}{\tau_{\text{col}}^2} (\pi^2 + \ln(e)^2), \quad (2.12)$$

$$\eta = -2\ln(e) \frac{\sqrt{m_{ab}k}}{\sqrt{\pi^2 + \ln(e)^2}}. \quad (2.13)$$

The radius of influence, λ , allows us to robustly handle high-speed collisions by initiating the collision of high-speed particle pairs just before contact. Following Finn *et al.* (2016), λ is calculated as

$$\lambda = \frac{\lambda_0}{2} (d_{p,a} + d_{p,b}) \left(\frac{\text{CFL}_{ab}^c}{\text{CFL}_{\max}^c} \right), \quad (2.14)$$

where the collisional CFL number is $\text{CFL}_{ab}^c = (2|\mathbf{u}_{ab,n}| \Delta t) / (d_p^a + d_p^b)$ and λ_0 is the maximum radius of influence permitted when the collision occurs at the maximum collision CFL number, CFL_{\max}^c . The tangential collision force is modeled according to a static friction model,

$$\mathbf{f}_{p,t}^{\text{c,b} \rightarrow \text{a}} = -\mu_s |\mathbf{f}_{p,t}^{\text{c,b} \rightarrow \text{a}}| \mathbf{t}_{ab} \quad (2.15)$$

where \mathbf{t}_{ab} is the tangential direction, and μ_s is the static friction coefficient. Collisions with walls are treated in the same way as above, but with the wall having infinite mass.

Note that the governing equations (2.1) and (2.2) for the fluid phase are solved in both simulations with particles and without. In the latter case, $\alpha_f = 1$ throughout the domain, which recovers the standard Navier-Stokes equations.

The solid phase dynamics are coupled with the fluid phase dynamics through the momentum exchange field \mathbf{F}_p , and the volume fraction fields, α_f and α_p . We

Cases	Re_δ	ρ_p/ρ_f	Ga	KC	d_p/δ	Θ_{\max}
1	200	2.65	51.9	134.5	0.7435	$2.79 \cdot 10^{-2}$
2	400	2.65	51.9	269.0	0.7435	$4.23 \cdot 10^{-2}$
3	800	2.65	51.9	538.0	0.7435	$4.48 \cdot 10^{-2}$

Table 1: Summary of the non-dimensional parameters for the presents runs of an OBL over a sediment bed. The maximum Shields number is determined a posteriori from the bed shear stress as described in §4.2.

calculate these fields using

$$\mathbf{F}_p(\mathbf{x}, t) = \sum_{i=1}^N \mathbf{f}_p^{h,i}(t) g(||\mathbf{x} - \mathbf{x}_p^i||) \quad (2.16)$$

$$\alpha_p(\mathbf{x}, t) = \sum_{i=1}^N V_p g(||\mathbf{x} - \mathbf{x}_p^i||), \quad (2.17)$$

$$\alpha_f(\mathbf{x}, t) = 1 - \alpha_p(\mathbf{x}, t) \quad (2.18)$$

In these equations, g represents a Gaussian filter with width $\delta_f = 5d_p$. We study the influence of filter width on fluid statistics in appendix B, and show that the statistics are converged with respect to filter width at $\delta_f = 5d_p$. Additional details on the computation of these terms and validation of the computational strategy, can be found in (Capecelatro & Desjardins 2013a,b; Capecelatro *et al.* 2014; Rao & Capecelatro 2019) and in our recent work (Kasbaoui *et al.* 2019; Kasbaoui 2019; Shuai *et al.* 2022; Shuai & Kasbaoui 2022; Dave & Kasbaoui 2023; Shuai *et al.* 2024; Van Doren & Kasbaoui 2024).

3. Numerical experiments

3.1. Configuration

We consider the dynamics of an oscillatory boundary layer over a cohesionless particle bed at three Reynolds number $Re_\delta = 200, 400$, and 800 . A summary of the relevant non-dimensional parameters for each run is listed in table 1. In order to provide a baseline for comparisons with the sediment-laden cases, we also carry out companion simulations at the same Reynolds numbers but with a bottom smooth and impermeable wall instead of a particle bed (see appendix A). Note that, without the particle bed, the flow at $Re_\delta = 200$ and 400 is in the laminar regime (see appendix A). We do not observe a disturbed laminar regime in these simulations due to the wall being smooth and flat and the absence of any external disturbances. The flow at $Re_\delta = 800$ falls in the intermittent turbulent regime. Comparing the simulations with and without a bottom particle bed helps elucidate the impact of sediment motion, bedforms, and bed permeability on the flow statistics.

In addition to the Reynolds number Re_δ , the presence of particles introduces additional dimensionless parameters. These are: (i) the density ratio ρ_p/ρ_f , (ii) the Galileo number $Ga = d_p \sqrt{(\rho_p/\rho_f - 1)gd_p}/\nu$, and the (iii) and the Keulegan-Carpenter number, $KC = U_0/\omega d_p$. Although not an independent number, the Shields number $\Theta_{\max} = \tau_{b,\max}/((\rho_p - \rho_f)gd_p)$, where $\tau_{b,\max}$ is the maximum bed shear stress, is also an important non-dimensional number to consider. The values for each case

Cases without bed	N_x 672	N_y 211	N_z 134	L_x/δ 250	L_z/δ 50	H_f/δ 61.9	H_b/δ 16.7
with bed	64	256	64	50	25	40	0

Table 2: Summary of domain parameters.

is shown in table 1. From a dimensional perspective, these cases correspond to an oscillating flow with period $T = 1.75$ s, velocity amplitude varying from $U_0 = 0.134$ m/s to 0.536 m/s, and sand particles with diameter 550 μm .

Finn *et al.* (2016) suggest that the regimes of particle transport is determined by the combination of Shields and Galileo numbers. Based on their work and the combination of the present parameters, case 1 ($Re_\delta = 200$) falls into the “no motion regime”. Cases 2 ($Re_\delta = 400$) and 3 ($Re_\delta = 800$) fall in the gravitational settling regime. We expect particle motion in both of these cases, with notably higher suspended sediment concentration in case 3 compared to case 2. In all these cases, the Keulegan-Carpenter number is very large, which suggests that inertial forces on particles caused by the unsteady flow oscillations are negligible compared to the drag force due to the instantaneous slip.

Figure 1 shows a schematic of the computational domain we use for the present simulations. Table 2 gives a summary of the computational parameters. The domain is long by 250δ in the streamwise direction and by 50δ in the spanwise direction. The domain height in the normal direction is $H_f + H_b$, where $H_f = 61.9\delta$ is the height of the clear fluid column and $H_b = 16.7\delta$ is the initial bed height. We chose the latter sufficiently deep ($H_b \sim 22d_p$) to accurately account for the flow intrusion within the bed. This gives a total number of particles $N = 6.09 \times 10^5$.

To discretize the governing equations, we use a uniform grid with spacing $\Delta x = d_p/2$ which provides a high resolution of the momentum coupling between and particle Eulerian fields such as particle volume fraction and velocity field. This results in a grid of size $672 \times 211 \times 134$. The timestep Δt is such that $\Delta t/T = 1.79 \times 10^{-5}$. This restrictive timestep is imposed by the requirement in the soft-sphere collision model that the bottom layer of the particles must support the weight of the particle bed above them. This is satisfied by ensuring that the spring stiffness in the collision model is sufficiently large to maintain a realistic volume fraction of 0.63 for a poured-bed (Scott & Kilgour 1969) (more details in (Capelat & Desjardins 2013a)). We use periodic boundary conditions in the streamwise and spanwise directions. In the wall-normal direction, we use far-field boundary conditions at the top, and no-slip condition at the bottom. Note that the bottom layer of particles is held fixed, whereas all other particles are free to move according to the evolution equations (2.5)–(2.7). In all cases, the particle restitution coefficient is maintained at 0.9 and the particle friction coefficient at 0.1.

The protocol to initialize the simulations and gathering statistics is as follows. We perform precursor simulations to generate a realistic poured-bed as described in §3.2. Then, we carry out simulations initialized from quiescent flow. We run the simulations for several periods until the flow reaches a periodic state and loses the effect of initial conditions. This takes about 2 periods. After this, we run the simulations for additional 8 periods to collect and compute phase-averaged statistics. We ensure that

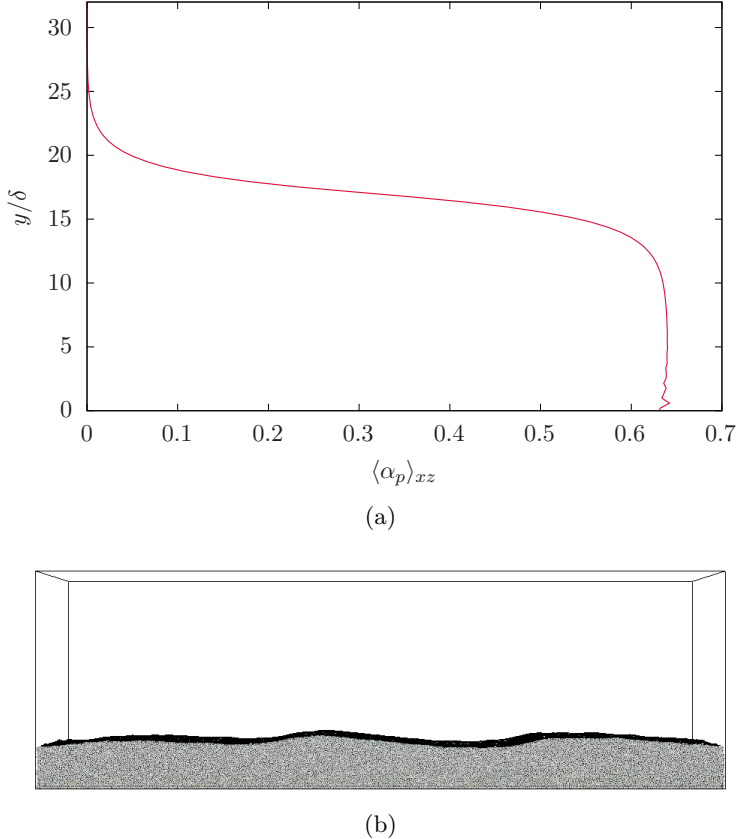


Figure 2: The particle bed is initialized by letting particles settle onto the bottom wall. (a) This procedure results in a volume fraction profile that is consistent with that of a poured bed. (b) The isosurface $\alpha_p = 0.2$ represents a good indicator of the location of the bed-fluid interface.

the statistics are converged by confirming that adding data from additional periods does not change the phase-averaged statics.

3.2. Bed formation and bed-fluid interface

To form the sediment bed, we perform precursor simulations that serve to generate a realistic bed volume fraction that matches the volume fraction of a poured bed, about 63% (Scott & Kilgour 1969). In these runs, the oscillatory forcing is turned off and the particles are initially uniformly distributed towards the middle of the domain at an average volume fraction of 40% and with small random velocity fluctuations. We then integrate the governing equations (2.1), (2.2), (2.5), (2.6), and (2.7) until the particles fully settle down. Particle-particle collisions and fluid-mediated particle-particle interactions lead to the formation of the poured bed in figure 1.

Figure 2a shows the average particle volume fraction $\langle \alpha_p \rangle_{xz}$ profile as a function of the wall normal distance. Note that here and onward, the notation $\langle \cdot \rangle_{xz}$ refers to ensemble and spatial averaging over the streamwise (x) and spanwise (z) directions. As anticipated, the volume fraction within the bed matches the random poured packing (Scott & Kilgour 1969). It smoothly transitions to zero away from the bed.

Further, we conduct the simulations with particle beds that are sufficiently deep to ensure that the interaction between the particle bed and the turbulent flow above is captured without interference from the bottom boundary. In the present study, the sediment bed is thick by about 22 particle diameters, which corresponds to about $\sim 16.7\delta$.

At this point, we must address the way we define the bed-fluid interface. We follow the approach of Kidanemariam & Uhlmann (2014), where we define the bed-fluid interface using an isosurface of the particle volume fraction $\alpha_p = \alpha_{p,b} < 0.63$. This is also similar to the experimental approach of Aussillous *et al.* (2013), where black white thresholding of sideview frames of the bed are used to detect the bed interface. However, it is important to recognize that the choice of the isosurface $\alpha_{p,b}$ demarcating the bed-fluid interface is somewhat arbitrary since the computation of the volume fraction field α_p depends on numerical choices. For example, the shape and size of the filter kernel used to compute α_p control the width of the transition region in figure 2a. With the filtering described in §2, the isosurface $\alpha_{p,b} = 0.2$ provides a good indicator of the approximate location of the bed-fluid interface. We determine this by verifying that this surface lies right on top of the particles as shown in figure 2b.

4. Characteristics of an oscillatory boundary layer over a cohesionless particle bed

Before proceeding further, we refer the reader to appendix A for a review of the flow features observed when the oscillatory boundary layer develops over a smooth and impermeable wall at $Re_\delta = 200, 400$, and 800 . These characteristics provide a benchmark for comparison in what follows. Having reviewed these dynamics, we now analyze the changes that occur when the oscillatory boundary layer develops over a cohesionless particle bed.

4.1. Overview of the dynamics

The presence of a sediment bed leads to notable vortex shedding, even at low Re_δ for which DNS of oscillatory boundary layers over smooth and impermeable walls show flow fields devoid of any fluctuations. At $Re_\delta = 200$, small waviness in the bed-fluid interface is responsible for vortex shedding. This is shown in figure 3 depicting the instantaneous spanwise vorticity in a wall normal plane at different phases of the cycle. To highlight the bedform, figure 3 also shows the volume fraction contour $\alpha_p = \alpha_{p,b} = 0.2$ that demarcates the sediment bed-fluid interface. The small waviness in the bed-fluid interface is the result of the initial bed generation as described in §3.2. At $Re_\delta = 200$, the bed shear stress is too low to induce any significant motion of the particles. Thus, the initial bedform persists throughout the simulation. The resulting flow fluctuations are reminiscent of the fluctuations described by Vittori & Verzicco (1998) in the disturbed laminar regime, where the bottom wall has small waviness. Since a smooth and impermeable wall does not generate such fluctuations at $Re_\delta = 200$ (see appendix A), this suggests that vortex shedding induced by asperities in the bed-fluid interface is the driving mechanics in the disturbed laminar regime.

At $Re_\delta = 400$, the particles in the bed's top layers become mobile. This leads to a dynamically evolving bed-fluid interface and greater vortex shedding, as shown in figure 4. Vortex shedding is strongest around phases 90° and 120° , i.e., from the maximum fluid velocity, and into the decelerating portion of the period. The

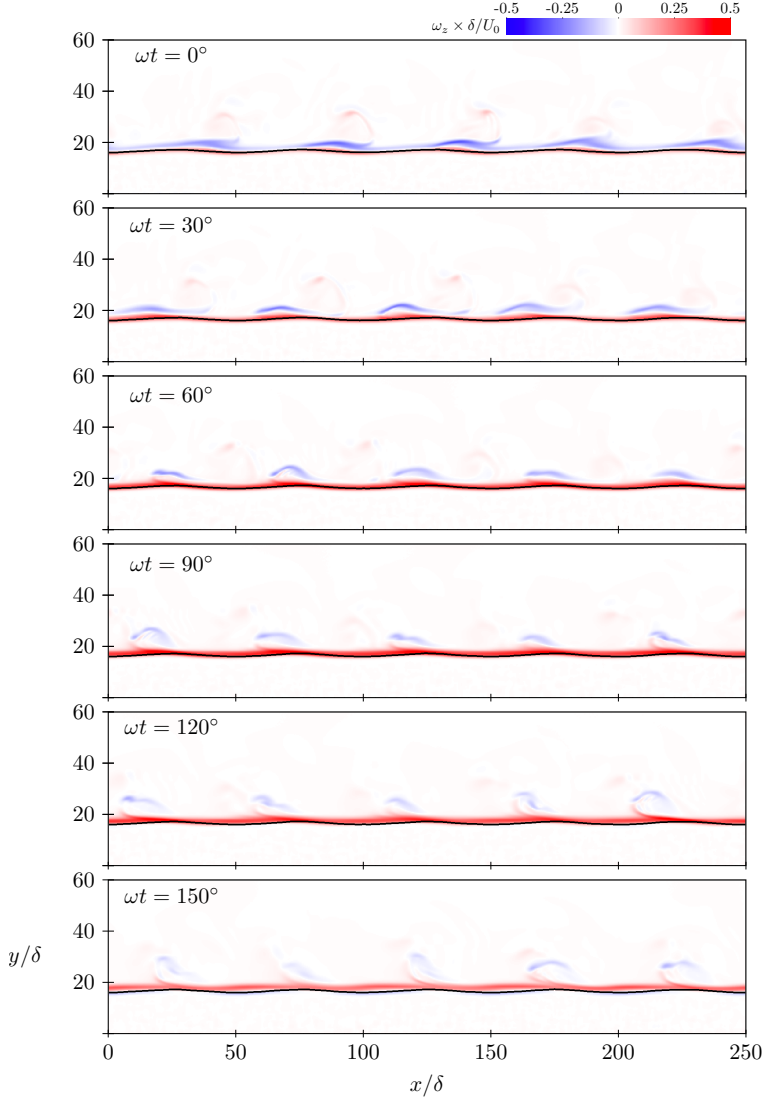


Figure 3: Zoomed-in view of the instantaneous spanwise vorticity and bed-fluid interface (solid line) at $Re_\delta = 200$. Small ripples in the bedform cause vortex shedding and fluctuations associated with the disturbed laminar regime.

vortex structures observed at these phases show a chaotic behavior, whereby larger structures spin off and break down into smaller ones. However, the range of scales is limited compared to what may be expected for a fully turbulent flow. The bed-fluid interface, marked by the black line in figure 4, changes dynamically with phase. This is due to particles being transported in the top layers of the bed, which couples the bedform dynamics to those of the flow over it.

We also note that bed permeability is significant at $Re_\delta = 400$. Whereas the extent of the flow intrusion below the bed-fluid interface is on the order of one Stokes thickness δ at $Re_\delta = 200$, the vortices generated at $Re_\delta = 400$ penetrate down by up to 4δ , judging from figures 3 and 4. Owing to the bed permeability, these vortices

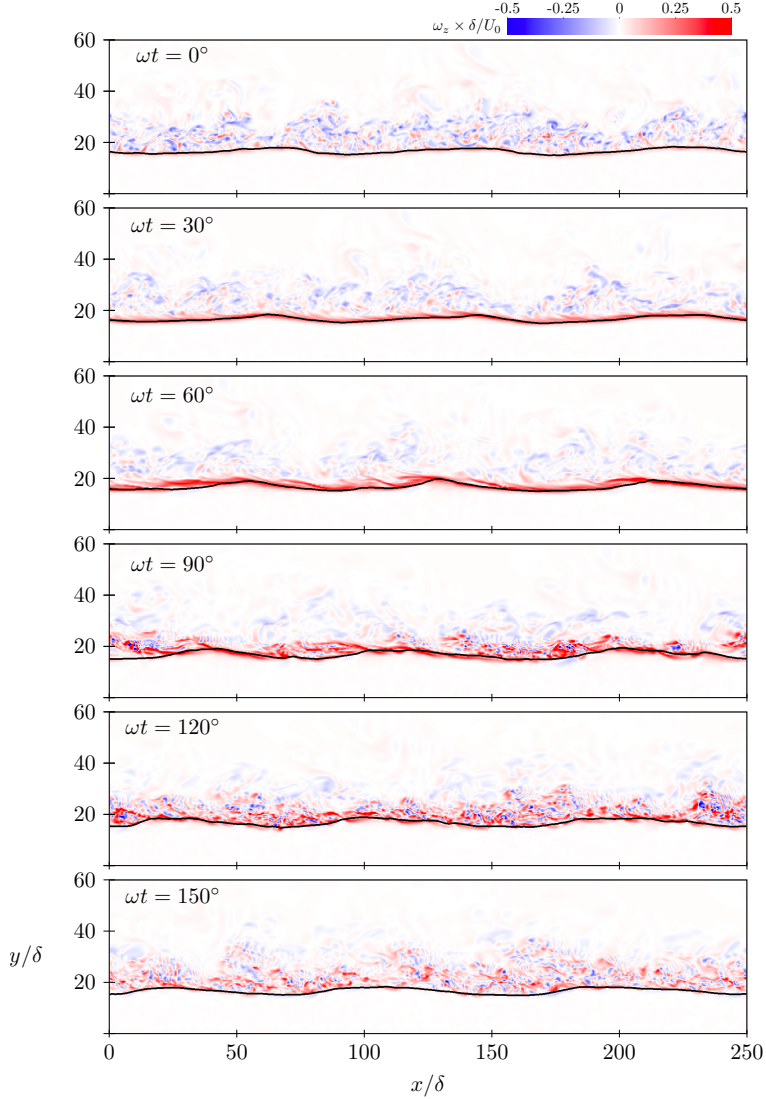


Figure 4: Zoomed-in view of the instantaneous spanwise vorticity and bed-fluid interface (solid line) at $Re_\delta = 400$. Increasing Reynolds number leads to greater vortex shedding and dynamically-evolving bed-fluid interface.

push fluid into and out of the bed. This plays an important role in the dynamic evolution of the bed-fluid interface, as flow exiting the bed exerts an upward drag force on the particles that helps suspend or set into motion particles in the bed's top layers (Jewel *et al.* 2019).

At $Re_\delta = 800$, figure 5 shows significant increase in flow disturbances over the bed, bed-fluid interface corrugations, and flow intrusion within the bed. The fluctuations' intensity and spatial extent exceed largely those due to intermittent turbulence in the case of an oscillatory boundary layer over a smooth and impermeable wall. The flow intrusion within the particle bed is also much greater at $Re_\delta = 800$ compared to $Re_\delta = 400$. This likely contributes to the increased corrugation of the bed-fluid

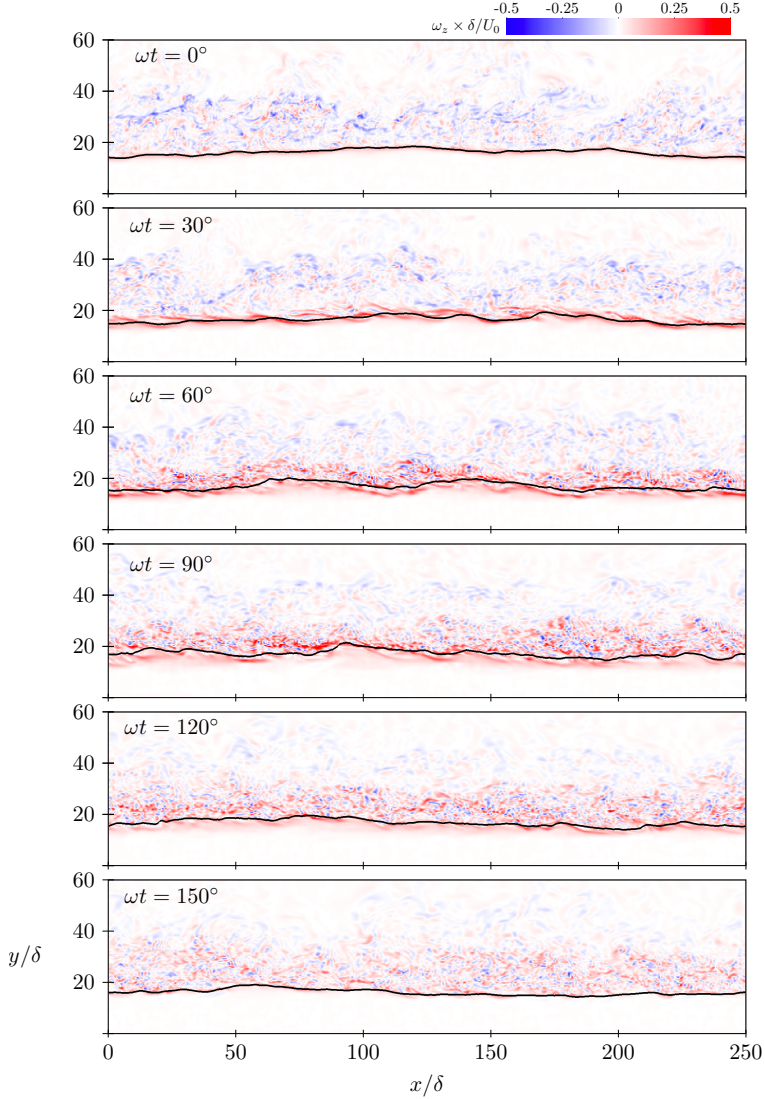


Figure 5: Zoomed-in view of the instantaneous spanwise vorticity and bed-fluid interface (solid line) at $Re_\delta = 800$. The bedform shifts into ripples at various phases. The shedding vortices create a large range of scales. The eddies penetrate the bed interface.

interface at this Reynolds number. Further, the bed-fluid interface is most corrugated around phases 60° , 90° , and 120° , which correspond to the phases with largest flow intrusion.

4.2. Fluid Statistics

Having established the qualitative dynamics of these flows in §4.1, we now characterize the fluid phase with quantitative measures.

Figure 6a, 6c, and 6e shows vertical profiles of phase-averaged mean streamwise fluid velocity $\langle u_f \rangle_{xz}$ from the cases with particle bed at $Re_\delta = 200$, 400, and 800. To better appreciate the change caused by the particle bed, we also report data from the

companion runs with a bottom smooth and impermeable wall discussed in appendix A. In this figure, y_b denotes the average bed height. We determine the latter by computing the average y location of the isovolume $\alpha = \alpha_b = 0.2$, which represents the bed-fluid interface.

At $Re_\delta = 200$, the average streamwise fluid velocity from the cases with a particle bed and smooth impermeable wall are sensibly close and follow the laminar Stokes solution. The notable differences include marginally thicker boundary layer, a significant slip velocity $u_{f,I}$ at the bed-fluid interface $y = y_b$, which reaches up to $u_{f,I} \simeq 0.25 U_0$ at phase 90° , and interstitial flow that decays quickly within 1.5δ of depth. These features are characteristic of permeable interfaces (Voermans *et al.* 2017), although their net effect on the average streamwise fluid velocity profiles at $Re_\delta = 200$ is limited.

With increasing Re_δ , the differences between cases with particle bed and cases with a smooth and impermeable wall accentuate as effects due to bed permeability effects increase. Most notably, we note the increase of the boundary layer thickness, interfacial slip velocity, and depth of the interstitial flow. At $Re_\delta = 400$, the interfacial slip velocity peaks at $u_{f,I} \simeq 0.29 U_0$ at phase 90° , while the flow extends below the bed-fluid interface by up to 4δ . At $Re_\delta = 800$, the maximum slip velocity increases to $u_{f,I} \simeq 0.42 U_0$ and the flow extends below the bed-fluid interface by up to 5δ .

In addition to altering the mean velocity profiles, the presence of a particle bed leads to greater velocity fluctuations than in the smooth wall cases. Figures 6b, 6d, and 6f show the streamwise velocity fluctuations for each Reynolds number. While the root mean square (rms) of the streamwise velocity fluctuations $u_{f,rms}$ in cases with smooth and impermeable wall at $Re_\delta = 200$ and 400 are identically zero, we note the existence of significant fluctuations in the cases with particle bed and at matching Reynolds numbers. For $Re_\delta = 200$, $u_{f,rms}$ peaks at about 13% of the velocity amplitude at about 0.18δ above the bed. At $Re_\delta = 400$, $u_{f,rms}$ rises to 27% of the velocity amplitude U_0 at phase 60° and about 0.56δ above the bed. At $Re_\delta = 800$, the $u_{f,rms}$ profiles are widest indicating that the flow disturbances extend to about 20δ to 30δ above the bed. The highest fluctuations occur at phase 60° and reach about 15% of the velocity amplitude.

The particle bed leads to a different condition at the fluid-bed interface as compared to a smooth wall. In the smooth wall case, no-slip applies at the wall, while the particle bed is porous, which leads to a slip velocity at the fluid-bed interface. This causes the bed shear stress to drop compared to the smooth wall case. We define the bed shear stress τ_b as the shear stress conditioned on an isosurface corresponding to the bed interface $\alpha_p = \alpha_{p,b}$. Figure 7 shows an example of instantaneous isosurface $\alpha = \alpha_b$ representing the bed-fluid interface. Formally, τ_b reads

$$\tau_b = \left\| \frac{1}{A_I} \iint_{S_I} \mathbf{n} \cdot \boldsymbol{\tau}' dS \right\| \quad (4.1)$$

where S_I represents the bed-fluid interface, A_I is the total interfacial area, \mathbf{n} is the normal vector on the isosurface $\alpha_p = \alpha_{p,b}$, and $\boldsymbol{\tau}' = \mu[\nabla \mathbf{u} + \nabla \mathbf{u}^T - (2/3)(\nabla \cdot \mathbf{u})\mathbf{I}] + \mathbf{R}_\mu$ is the deviatoric stress tensor. With the closure of Gibilaro *et al.* (2007), this tensor reads

$$\boldsymbol{\tau}' = \mu \alpha_f^{-2.8} \left(\nabla \mathbf{u} + \nabla \mathbf{u}^T - (2/3)(\nabla \cdot \mathbf{u})\mathbf{I} \right) \quad (4.2)$$

We define the coefficient of friction at the bed interface as

$$C_f = \frac{\tau_b}{(1/2)\alpha_{f,b}\rho_f U_0^2}. \quad (4.3)$$

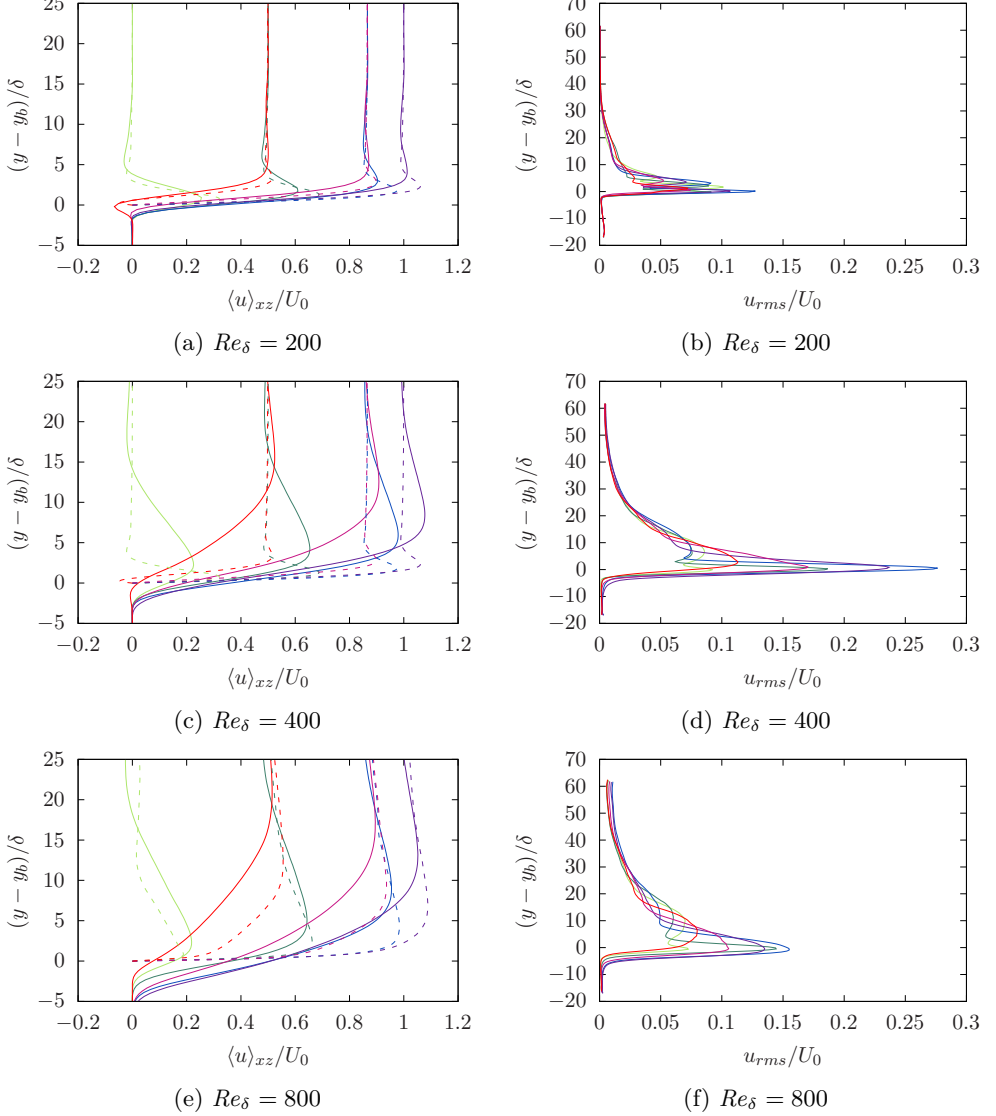


Figure 6: Statistics of the phase-averaged mean streamwise velocity at (a,b) $Re_\delta = 200$, (c,d) $Re_\delta = 400$, and (e,f) $Re_\delta = 800$. The lines correspond to phases $\omega t = 0$ (green), $\omega t = 30$ (black), $\omega t = 60$ (blue), $\omega t = 90$ (magenta), and $\omega t = 120$ (red). The dashed lines correspond to the smooth wall simulations from appendix A.

The coefficient of friction scaled by Re_δ is plotted in figure 8 as a function of time for each Reynolds number. For $Re_\delta = 200$ the coefficient is sinusoidal, with a phase shift of 15° compared to the single phase case. Additionally, the maximum coefficient of friction is reduced by 38.6%. At $Re_\delta = 400$, there is a turbulent eruption at $\omega t = 60^\circ$. We note that this is during the accelerating portion of the period, rather than in the decelerating portion of the period. The phase is shifted by 30° . The analytical phase shift for the coefficient of friction in the laminar regime is 45° , showing a departure even at low Reynolds number from the analytical behavior. The maximum coefficient

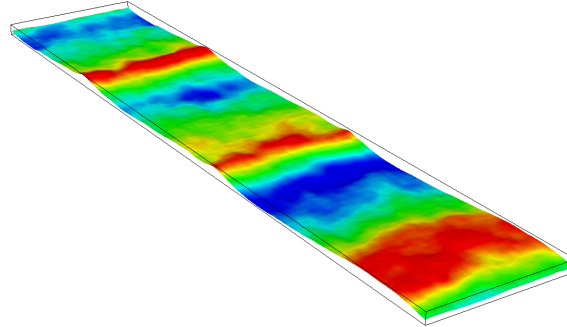


Figure 7: $Re_\delta = 400$ bedform height deviations. Small ripples rise and fall below the average bed height.

of friction is reduced by 53.1 %. The reduction in coefficient of friction is caused by the change in boundary condition near the wall, which leads to an inflection point in the streamwise velocity. The case at $Re_\delta = 800$ has a clear eruption of turbulence in the smooth wall case, as seen in the dramatic increase in coefficient of friction at phase 75°. The case with a particle bed does not show the same eruption of turbulence, rather, the coefficient of friction decreases at 45°, resulting in a sawtooth structure. Note that, while we have not measured the pressure drag from these present simulations, Mazzuoli *et al.* (2019) report that pressure drag, along side shear stress, could play a significant role in particle transport.

4.3. Particle Statistics

Next, we analyze the characteristics of the particulate phase and how these relate to those of the fluid phase.

At $Re_\delta = 400$, the particle bed is characterized by the periodic particle transport at the ripple crests. This can be seen in figure 9a which depicts a top-down view of the particle bed between $\omega t = 0^\circ$ and $\omega t = 150^\circ$ and where the particles are colored by their normalized streamwise velocities. At phase 0°, most particles are immobile and within the bed. From there, the rising fluid velocity initiates particle saltation at the ripple crests, which are well visible at phase 60°. These ripples are quasi-2D and display a wavelength of about $\sim 80\delta$. The rolling ripples continue intensifying until phase 90°. After that, the decrease in fluid velocity leads to a slow down of the particles until all are immobile again by phase 150°. This process occurs again, albeit in the reverse direction, between phases 180° and 320°.

With increasing Re_δ to 800, the particle transport enters the sheet flow regime (Hsu *et al.* 2004). As shown in figure 9b, the rolling ripples noted at $Re_\delta = 400$ are no longer present at $Re_\delta = 800$. Instead, we note the periodic emergence and collapse of a layer of suspended particles over the bed. At phase 0°, most particles start at rest in the bed. As the flow accelerates, particles in the top layer of the bed start saltating, which can be seen at phase 30°. As the fluid velocity continues increasing,

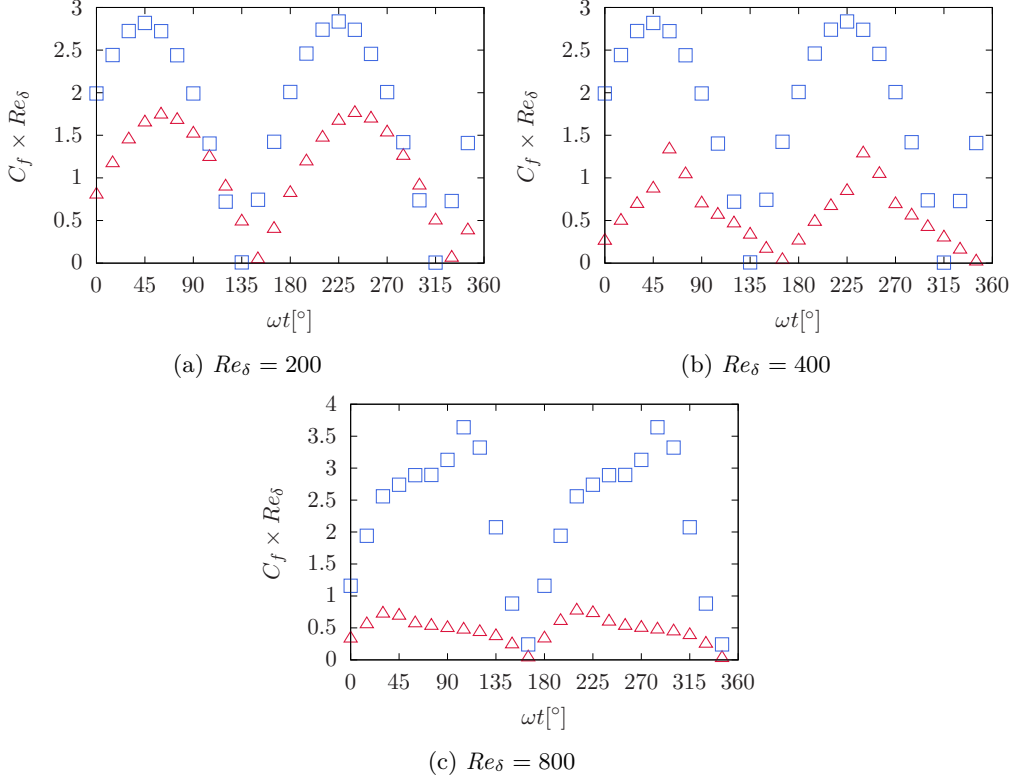


Figure 8: Coefficient of friction for an OBL over a particle bed. Red symbols corresponds to the particle bed case, blue symbols correspond to the smooth wall case. The coefficient of friction is reduced in amplitude by nearly half in the presence of a particle bed. The phase is shifted by 30° .

more particles are set in motion. At phase 60° , we note that a large number of particles are suspended within the fluid column. The sheet of suspended particles continues growing through phase 120° , by which point the fluid velocity has begun decreasing. With the continued slowing down of the flow, most particle redeposit in the bed by phase 150° , while only few remain suspended.

Note that we do not present similar figures to 9a and 9b for the case at $Re_\delta = 200$ because particle motion is negligible in that case.

Figure 10 shows the bed surface interface averaged over the spanwise direction, for $Re_\delta = 400$ and 800. The different lines correspond to the interface location from periods 2 to 10. At $Re_\delta = 400$, the bed-fluid interface in figure 10a develops into a clear bedform as the simulation progress. The wavelength associated with the ripples is $\lambda/\delta = 83.3$. The typical height of the ripples, measured from depression to peak, is about 4δ at phase 90° . While sediment particles move along the bed at significant velocities, as seen from figure 9a, the bedform evolves on a much slower periodic time scale. At $Re_\delta = 800$, the bed surface displays a range of small scale corrugations. However, the large scale ripples disappear. Figure 10b shows that the bed height deviations drop below 2δ . This is due to the fact that the rolling ripple mechanism is no longer the dominant mechanism for particle transport in the sheet flow regime.

Next, we report the vertical profiles of normalized particle momentum in figures 11a and 11b. At $Re_\delta = 400$, the normalized particle momentum is small, as

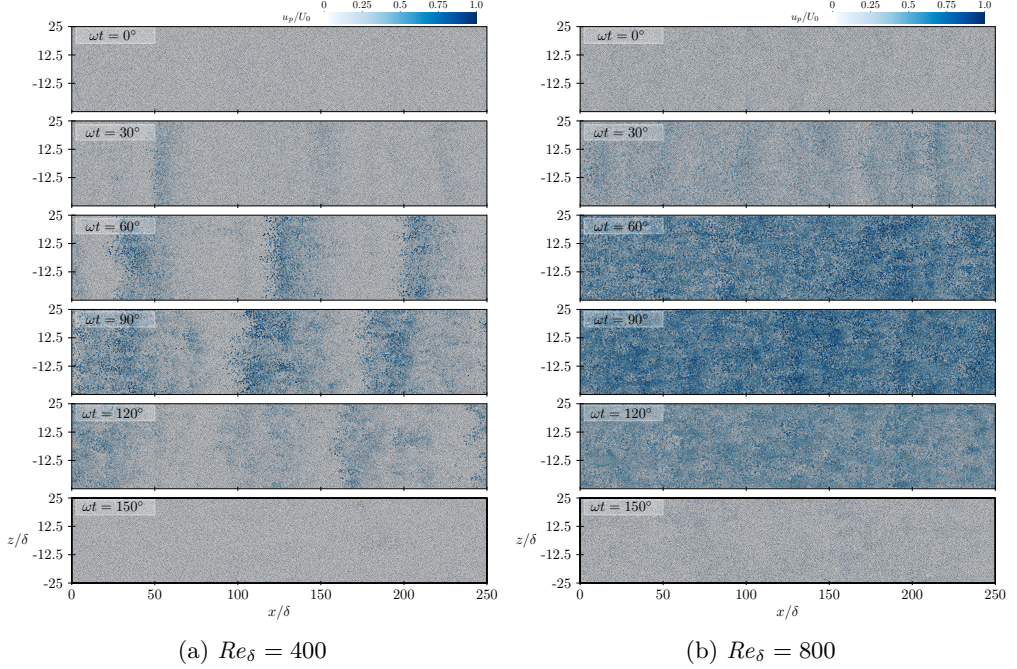


Figure 9: Top-down view of particle bed at phases 0° , 30° , 60° , 90° , 120° , 150° degrees for $Re_\delta = 400$ and 800 . The particles are colored by their normalized stream-wise velocity. The case at $Re_\delta = 400$ shows periodic rolling ripples, whereas the case at $Re_\delta = 800$ shows periodic sheet flow dynamics.

$\langle \rho_p \alpha_p u_p \rangle_{xz} / \rho_p U_0 < 0.025$ for all phases. This indicates that the rolling ripples move at a velocity much smaller than the fluid velocity amplitude U_0 . The largest particle momentum occurs at phase 150° , in agreement with the qualitative observations from figure 9a. We note that the particle momentum is non-zero only in a region of width $\sim 8\delta$ around the average bed height y_b . The width of this region is controlled by the height of the ripples, noted in figure 10a, and is not due to suspended particles, as the latter are negligible at $Re_\delta = 400$. In contrast, the normalized particle momentum reaches significantly higher values and displays wider distribution at $Re_\delta = 800$. At phase 150° , the region of non-zero particle momentum is about 18δ thick and peaks at about $0.08\rho_p U_0$. The widening of the profile and the absence of large scale deformations of the bed-fluid interface indicate that the amount of suspended particles is significantly larger at $Re_\delta = 800$ compared to $Re_\delta = 400$. This is also in agreement with the qualitative observations from figure 9b.

With regards to the computational aspects, we note that the particle momentum is negligible about $\sim 10\delta$ below the bed-fluid interface y_b at all phases and Re_δ considered. This shows that the particle bed in our simulations, which has an initial height $H_b = 16.7\delta$, is sufficiently tall to capture the dynamics near the bed-fluid interface without interference from boundary conditions at the bottom of the domain.

Figures 11c and 11d show the evolution of the normalized sediment flow rate q_s over a half period, for $Re_\delta = 400$ and 800 . We compute q_s by integrating the particle velocity profiles over the vertical direction, i.e.,

$$q_s = \int_0^{L_y} \langle \alpha_p u_p \rangle_{xz} dy. \quad (4.4)$$

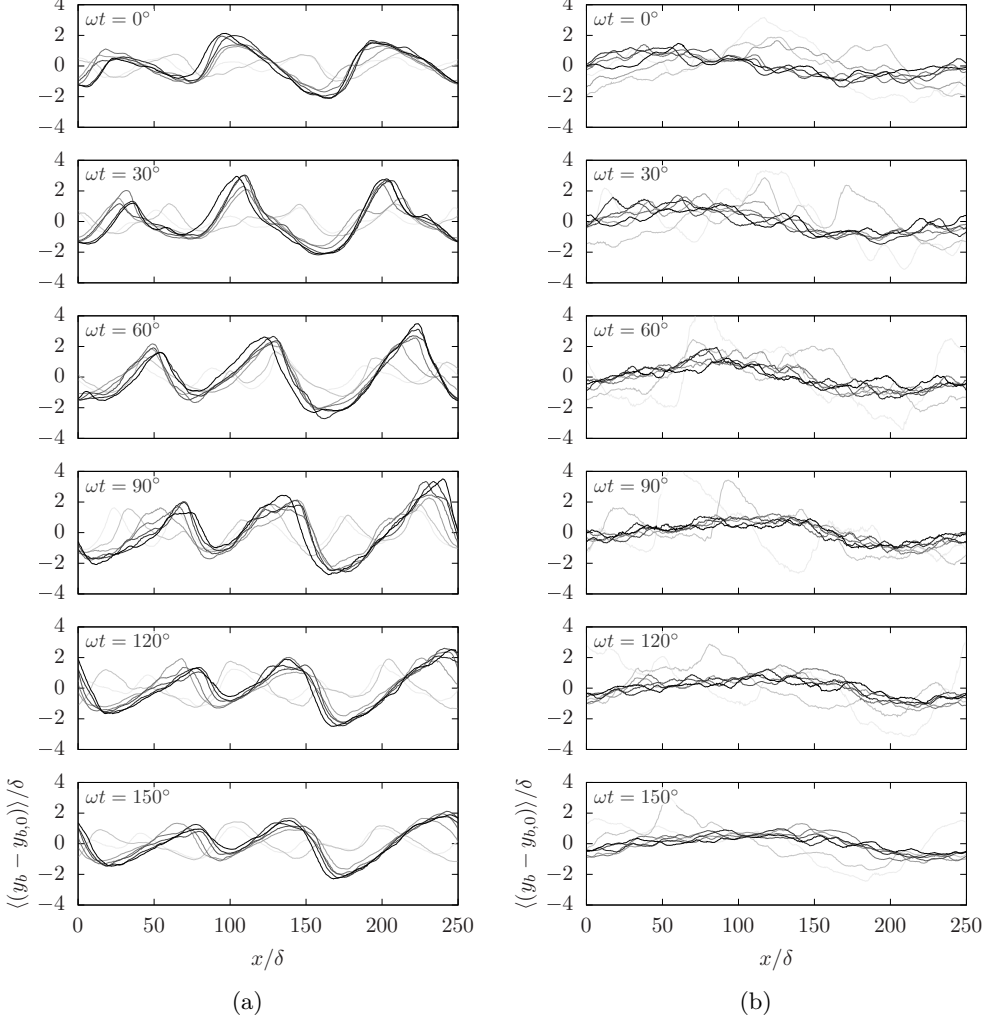


Figure 10: Bed interface for (a) $Re_\delta = 400$ and (b) $Re_\delta = 800$. Darker lines indicate later periods. For $Re_\delta = 400$, rolling grain ripples emerge and move through domain, but the dominant wavelength does not change. At $Re_\delta = 800$, the bed height becomes highly corrugated, and the bed fluid interface breaks down.

At $Re_\delta = 400$, the sediment volumetric flux peaks at 0.94 at phase $\omega t = 90^\circ$. Notably, the sediment transport is not symmetric for the accelerating and decelerating portions of the periods. At $Re_\delta = 800$, the sediment flux is more than 4 times greater than at $Re_\delta = 400$. The maximum normalized flux is 8.73 at phase 90° . Here too, we note an asymmetry between the acceleration and deceleration portions of the period.

5. Discussion and conclusions

In this study, we analyze data obtained from Euler-Lagrange simulations of an oscillatory boundary layer developing over a bed of collisional and freely moving

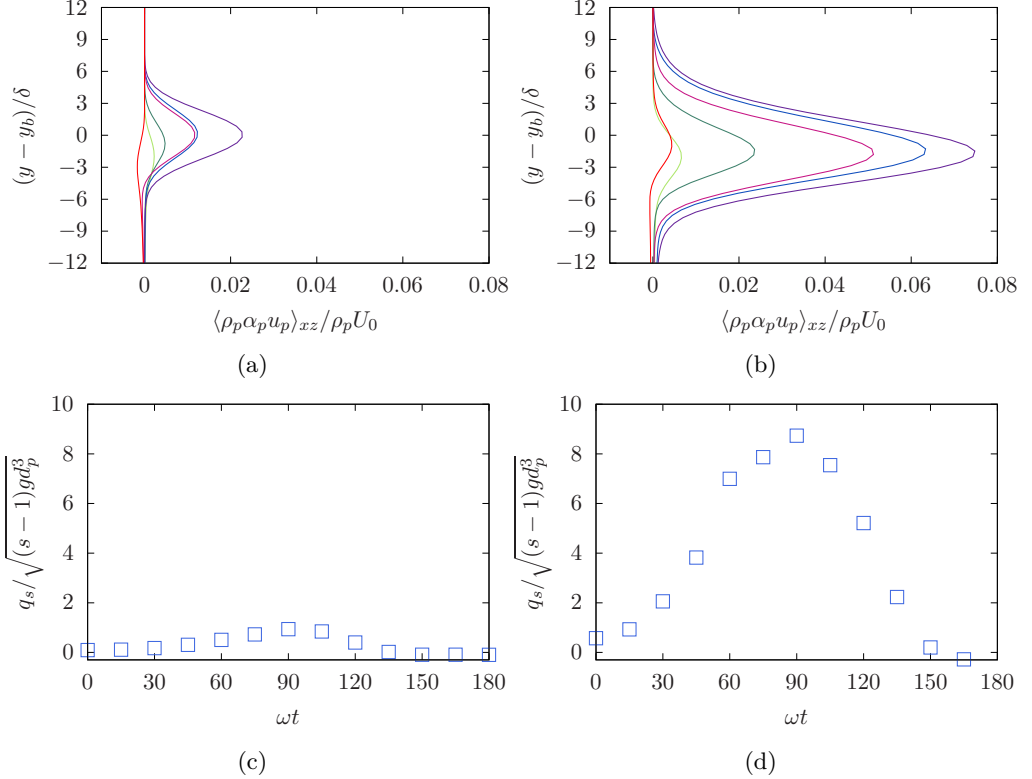


Figure 11: Normalized particle momentum profiles and mass fluxes at $Re_\delta = 400$ (a,c) and $Re_\delta = 800$ (b,d). The lines in (a,b) correspond to phases: $(\omega t = 0, \text{green}), (\omega t = 30, \text{cyan}), (\omega t = 60, \text{blue}), (\omega t = 90, \text{purple}), (\omega t = 120, \text{pink}), (\omega t = 150, \text{red})$. Significant particle momentum is seen near the bed interface, indicating particle motion at around the bed interface.

sediment grains with density ratio $\rho_p/\rho_f = 2.65$ and Galileo number $Ga = 51.9$. In these simulations, we vary the velocity amplitude to yield Reynolds numbers $Re_\delta = 200$ to 800. The maximum Shields number also varies from $2.79 \cdot 10^{-4}$ to $4.48 \cdot 10^{-4}$ and the Keulegan-Carpenter number varies from 134.5 to 538.0. Companion simulations of an oscillatory boundary layer over a smooth and impermeable wall show that the boundary layer follows the laminar Stokes solution at $Re_\delta = 200$ and $Re_\delta = 400$ and displays intermittent turbulence at $Re_\delta = 800$. However, the presence of a mobile bed alters the flow characteristics and leads to a coupling of the dynamics of the oscillatory boundary layer with those of the sediment bed.

The coupled dynamics arise from two fundamental mechanisms. The first one relates to the bed permeability. This is due to the porosity of the bed which allows the flow to penetrate within the sediment layers. The extent of the flow penetration depends on the Reynolds number. In the case at $Re_\delta = 200$, the flow penetration is on the order of the Stokes thickness δ . With increasing Re_δ , the flow penetration increases to about 4δ and 5δ at $Re_\delta = 400$ and $Re_\delta = 800$, respectively. Another consequence of the bed permeability is the emergence of a slip velocity at the bed-fluid interface. At phase 90° of the cycle, the interfacial slip velocity peaks at about $0.25U_0$, $0.292U_0$, and $0.42U_0$, at $Re_\delta = 200$, 400, and 800, respectively. This significant slip leads to a thickening of the boundary layer and reduction of the bed shear stress.

The maximum Shields number in the case at $Re_\delta = 200$ is 38% lower than the one found with a bottom impermeable wall. At $Re_\delta = 400$ and 800, the maximum Shields number drops further by 54% and 79%, respectively.

The second fundamental mechanism that couples the dynamics of the particle bed and the oscillatory boundary layer relates to particle motion. In the case at $Re_\delta = 200$, the particles remain immobile during the entire cycle. This is expected because the maximum Shields number in this case ($\Theta_{\max} = 2.79 \cdot 10^{-2}$) is below the critical Shields number for incipient motion. Thus, the only changes to the oscillatory boundary layer in this case are those due to permeability. At $Re_\delta = 400$ and 800, the particles become mobile and lead to a dynamic evolution of the sediment bed. At $Re_\delta = 400$, the particles form rolling-grain ripples. The latter emerge from small scale corrugations in the bed-fluid interface. These corrugations coarsen very quickly and lead to a bedform with height 4δ and wavelength of about $\sim 80\delta$. Analyzing the vorticity dynamics shows that these ripples cause enhanced vortex shedding in the flow which leads to fluid velocity disturbances similar to those observed in the disturbed laminar regime. At $Re_\delta = 800$, the sediment bed enters the sheet flow regime. Between phases 60° and 120° of the half-cycle, the bed-fluid interface recedes slightly and a layer of suspended particles forms. During the rest of the half-cycle, the suspended particles settle into the bed and become nearly motionless at phase 0° . Because of their large momentum and their feedback force on the fluid, the suspended particles induce significant fluctuations in the flow. This leads to further widening of the boundary layer and greater fluctuations than is observed in the corresponding particle-free case.

In this work, we have also shown that the dynamics of sediment beds under a wide range of oscillatory and unsteady flow conditions can be predicted at reasonable computational cost using carefully designed Euler-Lagrange simulations. While PR-DNS require little to no models, their large computational cost often makes them too restrictive. In comparison with the PR-DNS of Mazzuoli *et al.* (2020), our simulations have domains 100 times larger: about 10 times longer in the streamwise direction, about 4 times wider in the spanwise direction, and about twice taller. This allows us to capture bedforms which was not possible in (Mazzuoli *et al.* 2020). Further, we were able to simulate 10 cycles for each of our cases, compared to 1 to 4 cycles in (Mazzuoli *et al.* 2020). The computational cost of these simulations is about 400,000 CPU-hours per case (equivalent to about 15 day run time on 1152 CPUs), which is attainable for many researchers with today's computational resources.

Acknowledgements. Computing resources through ACCESS award EES230041 and Research Computing at Arizona State University are gratefully acknowledged.

Funding. This research received no specific grant from any funding agency, commercial or not-for-profit sectors.

Declaration of interests. The authors report no conflict of interest.

Author ORCIDs. M. H. Kasbaoui, <https://orcid.org/0000-0002-3102-0624>;

Appendix A. Structure of an Oscillatory Boundary Layer over a smooth wall

In this appendix, we present a detailed description of the flow characteristics at $Re_\delta = 200$, 400, and 800, where the bottom boundary is an impermeable smooth wall rather than a sediment bed. The reasons for this are twofold. First, analytical solutions exist for the laminar regime, which allows the validation of the computational approach.

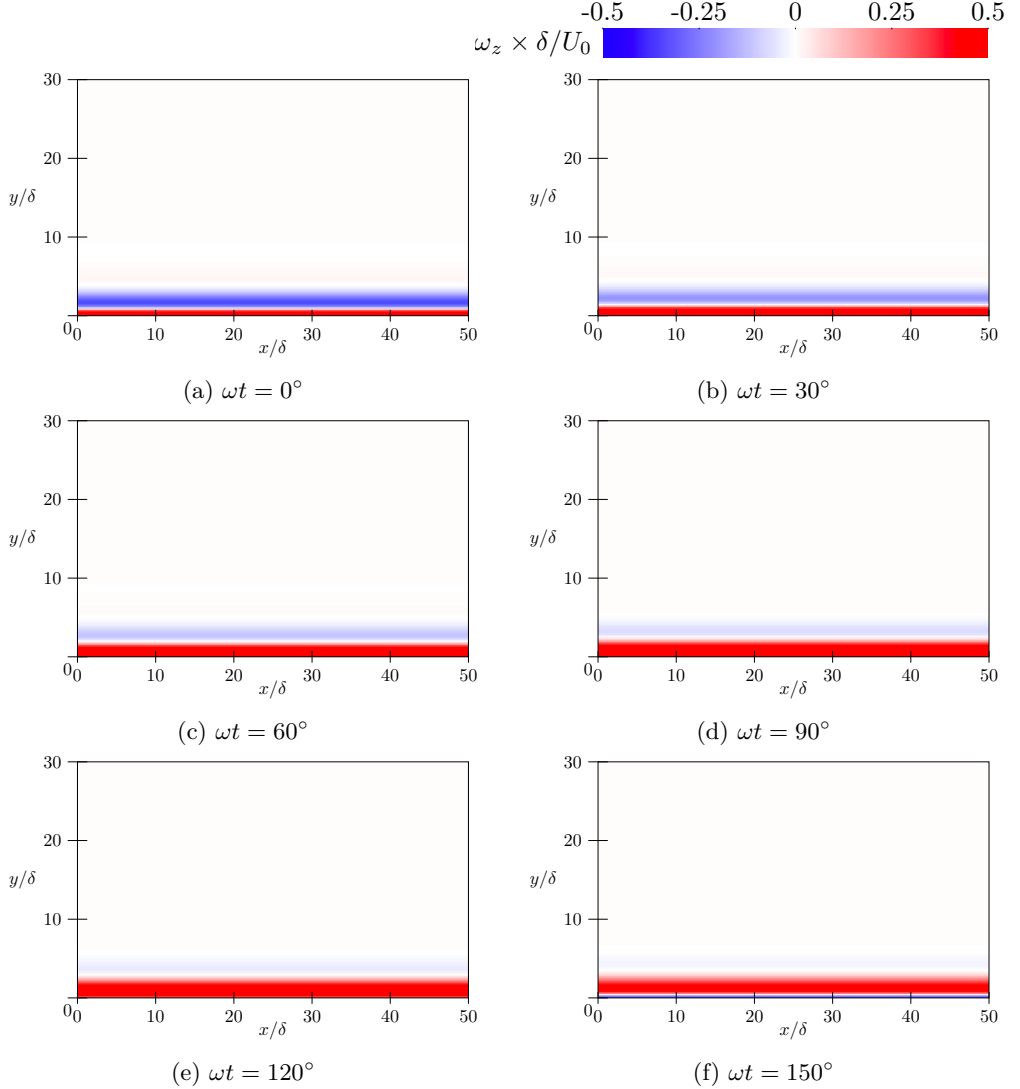


Figure 12: Normalized spanwise vorticity fields at $Re\delta = 400$ for a smooth, impermeable wall, at phases 0, 30, 60, 90, 120 and 150 degrees. The vorticity is arranged in laminae at all phases.

Second, these runs serve as benchmark to elucidate the changes to the flow in presence of a sediment bed.

Figure 12 shows the normalized spanwise vorticity field at phases $\omega t = 0^\circ$, 60° , 90° , 120° , and 180° for the case $Re\delta = 400$. The solution for $Re\delta = 200$ shows similar vorticity structure to the $Re\delta = 400$ solution and, thus, is not included here. The vorticity in these low Reynolds number cases, is organized into sheets in the near-wall region. This indicates laminar flow, and so the flow at $Re\delta = 200, 400$ should obey the Stokes solution,

$$u_{f,x}/U_0 = \cos(\omega t) - e^{-y/\delta} \cos(\omega t - y/\delta), \quad (A 1)$$

$$u_{f,y}/U_0 = 0. \quad (A 2)$$

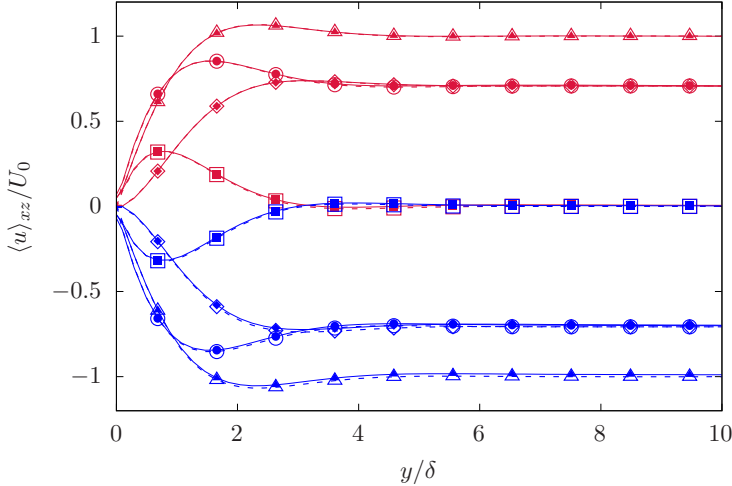


Figure 13: Normalized stream-wise velocity for the case of an OBL over an impermeable smooth wall at $Re_\delta = 400$. Filled symbols correspond to the Stokes solution, while open symbols correspond to smooth wall simulations. To differentiate the positive and negative portions of the period, we plot the positive half cycle in red and the negative half cycle in blue. The symbols indicate the phase: (\square , $\omega t = 0^\circ, 180^\circ$), (\circ , $\omega t = 45^\circ, 225^\circ$), (\triangle , $\omega t = 90^\circ, 270^\circ$), (\diamond , $\omega t = 135^\circ, 315^\circ$). The strong agreement between the simulated data and the Stokes solution indicates that the flow is fully laminar in this case.

To verify this, we compare the Stokes solution to vertical profiles of the phase-averaged fluid velocity from the simulation at $Re_\delta = 400$ in figure 13. The agreement between the simulated data and the analytical solution is excellent, showing that the flow is indeed laminar at these Reynolds numbers. This also validates the computational approach for an impermeable smooth wall oscillatory boundary layer at low Reynolds numbers.

As an additional comparison, we compute the coefficient of friction C_f defined as,

$$C_f = \frac{|\tau_w|}{(1/2)\rho_f U_0^2}, \quad (\text{A 3})$$

where τ_w is the wall shear stress. Figure 14 shows the variation of the coefficient of friction scaled by Re_δ to cancel the Reynolds number dependence of the coefficient of friction. The scaled coefficient is plotted over a period for the cases of an OBL over an impermeable smooth wall at $Re_\delta = 200$ and 400 , alongside the Stokes solution. Here too, the agreement between numerical and Stokes solution is excellent which further demonstrates that the OBL at these Reynolds number is fully laminar.

Unlike the lower Reynolds number cases, figure 15 shows significant vorticity throughout the cycle for the case at $Re_\delta = 800$. Of particular interest is the range of scales seen at phase 120° , which is in the decelerating portion of the cycle. This eruption of velocity fluctuations, followed by partial relaminarization, is characteristic of the intermittent turbulence regime. Similar observations were made by Jensen *et al.* (1989), Vittori & Verzicco (1998), and Salon *et al.* (2007).

While the vorticity field for $Re_\delta = 800$ shows a range of eddies, strict wall-bounded turbulence requires the existence of a logarithmic layer. To this end, we report in figure 16 vertical profiles of the spatially averaged streamwise velocity normalized

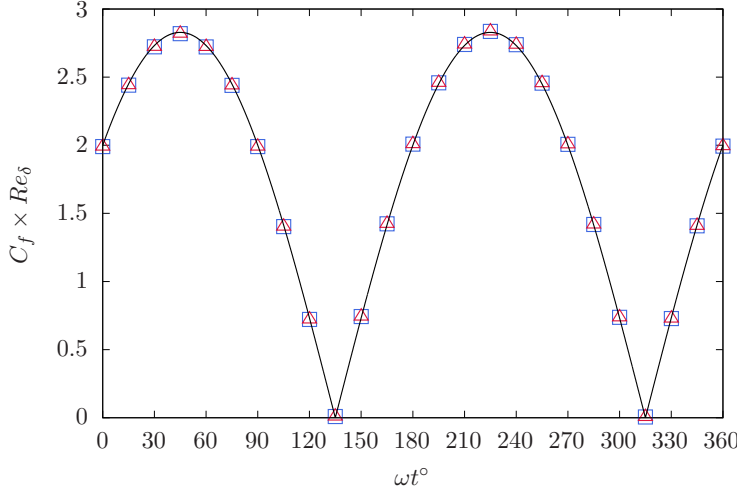


Figure 14: Scaled coefficient of friction over one period at $Re_\delta = 200$ and 400 , for a smooth, impermeable wall. The black line correspond to the Stokes solution. Symbols correspond to the numerical solution at ($\square, Re_\delta = 200$) and ($\triangle, Re_\delta = 400$). All cases collapse onto the Stokes solution.

using wall units, i.e., the friction velocity $u_\tau = \sqrt{\tau_w/\rho_f}$ as velocity scale and ν/u_τ as length scale. Since none of the phases show a strict logarithmic layer, we conclude that the flow at $Re_\delta = 800$ is not fully turbulent, despite presenting significant fluctuations.

Appendix B. Analysis of filter width

In Eulerian-Lagrange simulations, the choice of filter width δ_f is an important modeling consideration. To justify the point-particle approximation δ_f must be much larger than the particle size d_p . Yet, resolving the vortical structures requires δ_f to also be as small as possible. For the present study, we chose $\delta_f = 5d_p$. As recently shown in (Hausmann *et al.* 2024), this filter size reduces errors associated with the point-particle approximation, while providing adequate resolution.

To show the impact of filter size on the fluid statistics, we performed additional simulations of the case at $Re_\delta = 800$ with filter sizes $\delta_f = 3d_p$, $5d_p$, and $7d_p$. Note that $\delta_f = 3d_p$ is generally considered to be too small to justify the point-particle approximation, while $\delta_f = 5d_p$ and $\delta_f = 7d_p$ are values commonly used in the literature (Capelat & Desjardins 2013a; Hausmann *et al.* 2024).

Figure 17 shows the impact of varying the filter size on mean and rms fluctuations of the streamwise velocity at phases 0° , 90° , and 150° . We note that, as expected, $\delta_f = 3d_p$ shows the largest deviation. The results at $\delta_f = 5d_p$ and $\delta_f = 7d_p$ are sensibly similar, which justifies our choice of $\delta_f = 5d_p$ for the remaining simulations.

The reader interested in further details on the role of filter size in Euler-Langrange modeling is referred to (Hausmann *et al.* 2024).

REFERENCES

AKHAVAN, R., KAMM, R. D. & SHAPIRO, A. H. 1991a An investigation of transition to

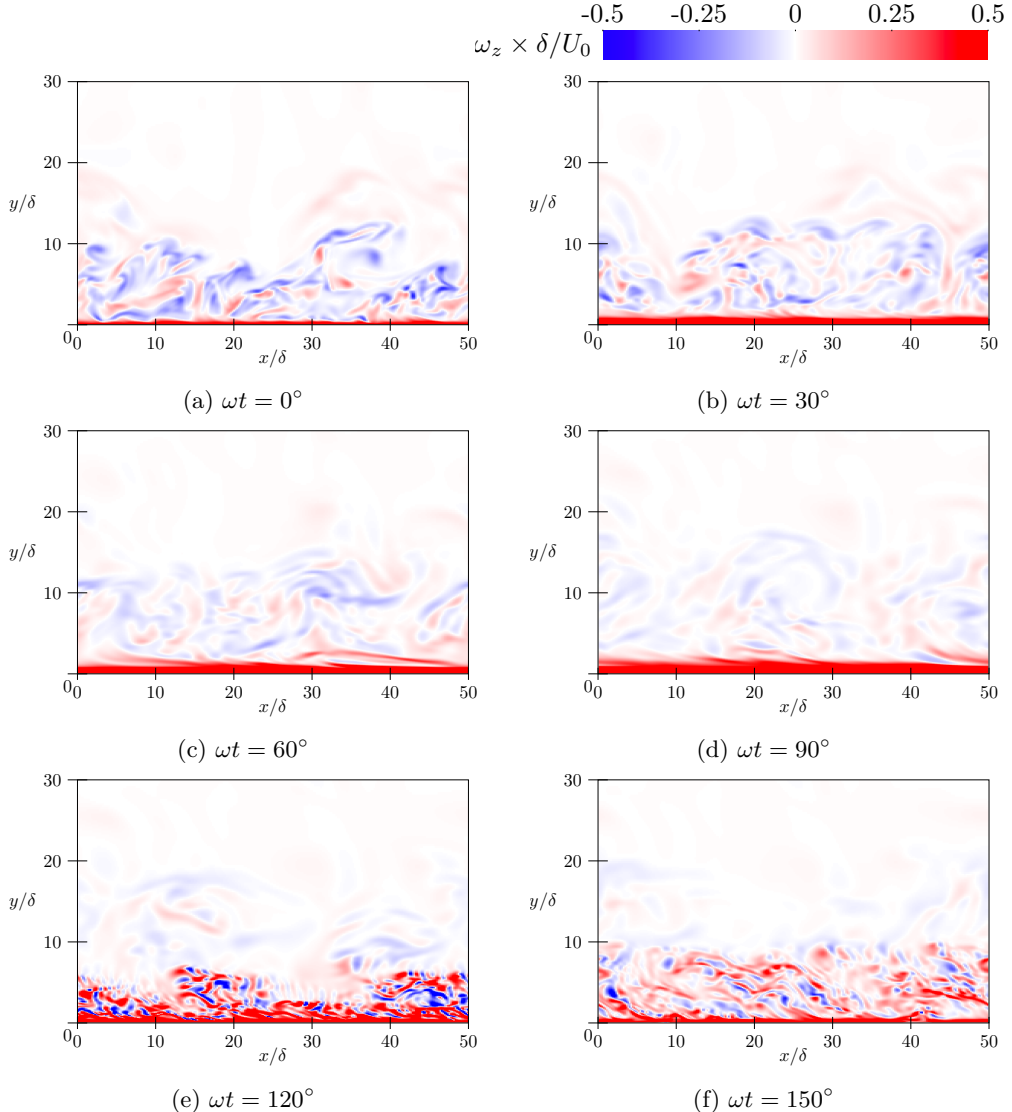


Figure 15: Normalized spanwise vorticity field in DNS of an OBL over an impermeable smooth wall at $Re_\delta = 800$, for a smooth, impermeable wall. The eruption of velocity fluctuations during the decelerating portion of the cycle (120° and 150°) indicates that this flow is in the intermittent turbulent regime.

turbulence in bounded oscillatory Stokes flows Part 1. Experiments. *Journal of Fluid Mechanics* **225**, 395–422.

AKHAVAN, R., KAMM, R. D. & SHAPIRO, A. H. 1991b An investigation of transition to turbulence in bounded oscillatory Stokes flows Part 2. Numerical simulations. *Journal of Fluid Mechanics* **225**, 423–444.

ANDERSON, T. B. & JACKSON, R. 1967 Fluid Mechanical Description of Fluidized Beds. Equations of Motion. *Industrial & Engineering Chemistry Fundamentals* **6** (4), 527–539.

APTE, SOURABH V., MARTIN, MATHIEU & PATANKAR, NEELESH A. 2009 A numerical method for fully resolved simulation (FRS) of rigid particle–flow interactions in complex flows. *Journal of Computational Physics* **228** (8), 2712–2738.

AROLLA, S. K. & DESJARDINS, O. 2015 Transport modeling of sedimenting particles in a

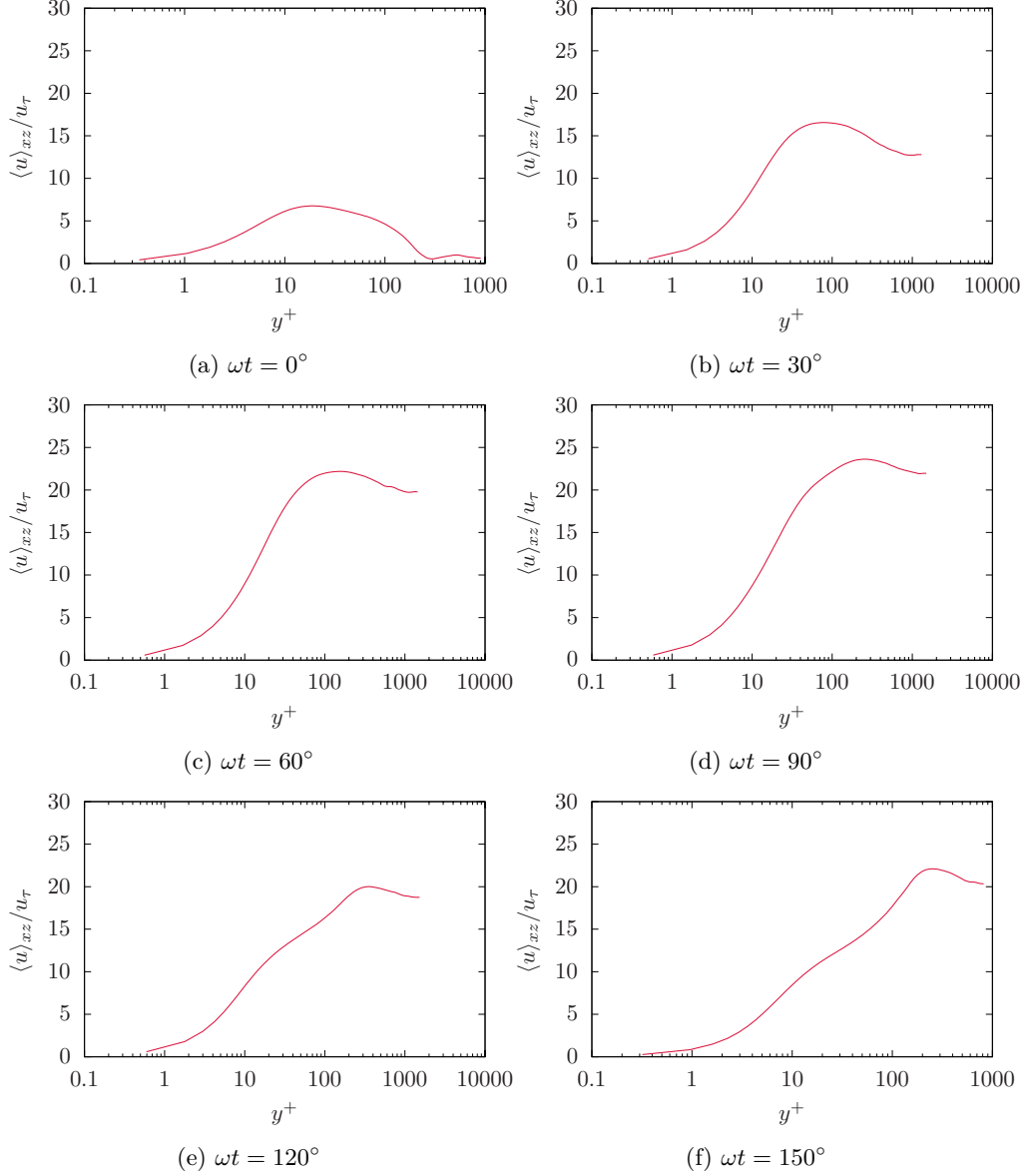


Figure 16: Wall scaled mean velocity profiles for $Re_\delta = 800$, for a smooth, impermeable wall. No logarithmic layer is observed.

turbulent pipe flow using Euler–Lagrange large eddy simulation. *International Journal of Multiphase Flow* **75**, 1–11.

AUSSILLOUS, PASCALE, CHAUCHAT, JULIEN, PAILHA, MICKAEL, MÉDALE, MARC & GUAZZELLI, ÉLISABETH 2013 Investigation of the mobile granular layer in bedload transport by laminar shearing flows. *Journal of Fluid Mechanics* **736**, 594–615.

BLONDEAUX, P. & SEMINARA, G. 1979 Transizione incipiente al fondo di un’onda di gravità. *Atti della Accademia Nazionale dei Lincei. Classe di Scienze Fisiche, Matematiche e Naturali. Rendiconti* **67** (6), 408–417.

BREUGEM, WIM-PAUL 2012 A second-order accurate immersed boundary method for fully

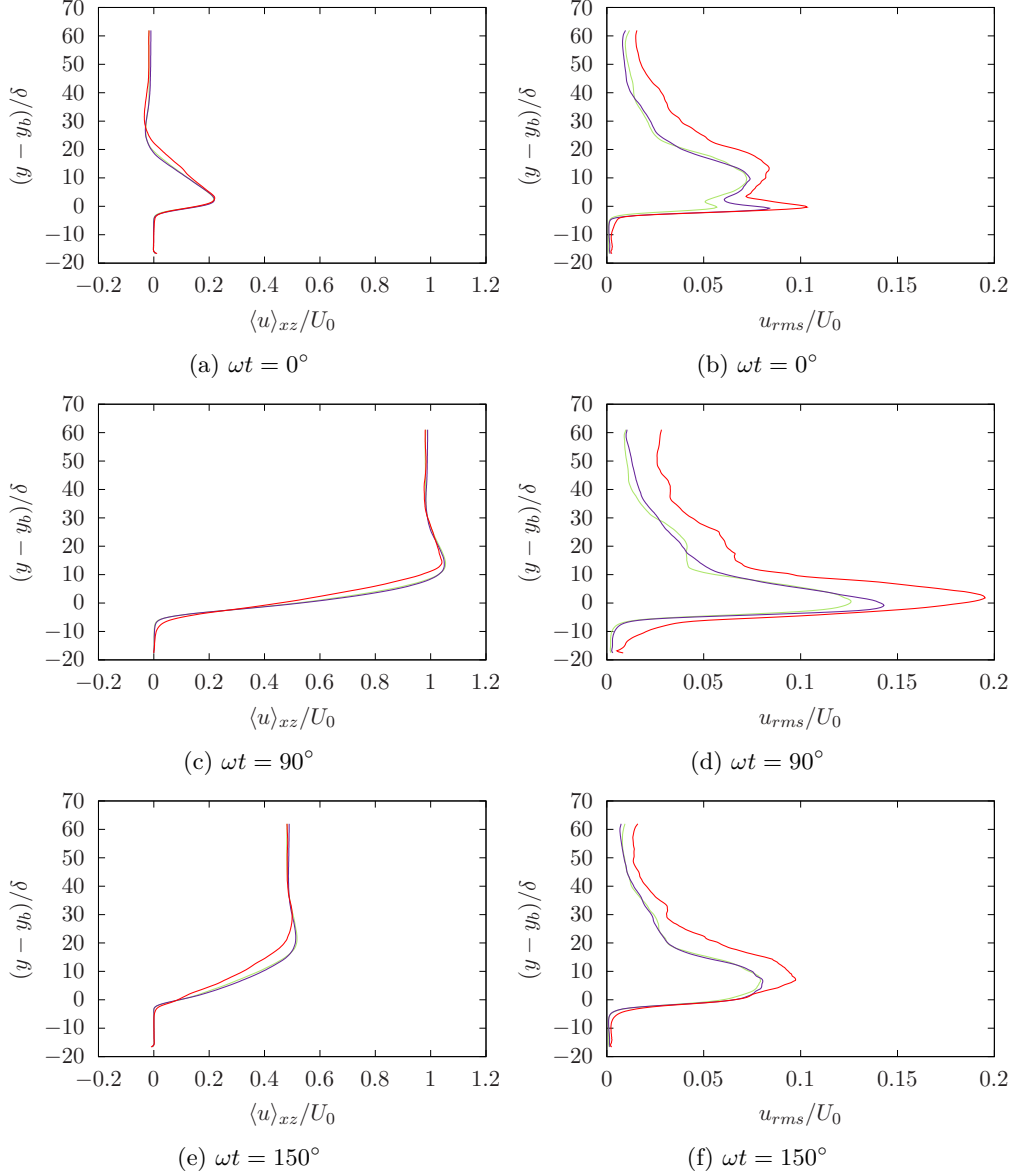


Figure 17: Statistics of the streamwise fluid velocity for filter widths $\delta_f = 3d_p$ (red), $5d_p$ (blue), and $7d_p$ (green): (a,c,e) mean and (b,d,f) rms fluctuations.

There is little difference between results with $\delta_f = 5d_p$ and $\delta_f = 7d_p$, which indicates that either values are a good choice in Euler-Lagrange simulations.

resolved simulations of particle-laden flows. *Journal of Computational Physics* **231** (13), 4469–4498.

BREUGEM, W. P., BOERSMA, B. J. & UITTENBOGAARD, R. E. 2006 The influence of wall permeability on turbulent channel flow. *Journal of Fluid Mechanics* **562**, 35.

CAPECELATRO, J. & DESJARDINS, O. 2013a An Euler–Lagrange strategy for simulating particle-laden flows. *Journal of Computational Physics* **238**, 1–31.

CAPECELATRO, J. & DESJARDINS, O. 2013b Eulerian–Lagrangian modeling of turbulent liquid–solid slurries in horizontal pipes. *International Journal of Multiphase Flow* **55**, 64–79.

CAPECELATRO, JESSE, PEPIOT, PERRINE & DESJARDINS, OLIVIER 2014 Numerical characterization and modeling of particle clustering in wall-bounded vertical risers. *Chemical Engineering Journal* **245**, 295–310.

CARSTENSEN, S., SUMER, B. M. & FREDSØE, J. 2010 Coherent structures in wave boundary layers. Part 1. Oscillatory motion. *Journal of Fluid Mechanics* **646**, 169–206.

CARSTENSEN, S., SUMER, B. M. & FREDSØE, J. 2012 A note on turbulent spots over a rough bed in wave boundary layers. *Physics of Fluids* **24** (11), 115104.

CONLEY, DANIEL C. & INMAN, DOUGLAS L. 1994 Ventilated oscillatory boundary layers. *Journal of Fluid Mechanics* **273**, 261–284.

COSTAMAGNA, P., VITTORI, G. & BLONDEAUX, P. 2003 Coherent structures in oscillatory boundary layers. *Journal of Fluid Mechanics* **474**, 1–33.

DAVE, HIMANSHU & KASBAOUI, M. HOSSEIN 2023 Mechanisms of drag reduction by semidilute inertial particles in turbulent channel flow. *Physical Review Fluids* **8** (8), 084305.

FINN, J. R. & LI, M. 2016 Regimes of sediment-turbulence interaction and guidelines for simulating the multiphase bottom boundary layer. *International Journal of Multiphase Flow* **85**, 278–283.

FINN, J. R., LI, M. & APTE, S. V. 2016 Particle based modelling and simulation of natural sand dynamics in the wave bottom boundary layer. *Journal of Fluid Mechanics* **796**, 340–385.

FYTANIDIS, D. K., GARCÍA, M. H. & FISCHER, P. F. 2021 Mean flow structure and velocity–bed shear stress maxima phase difference in smooth wall, transitionally turbulent oscillatory boundary layers: Direct numerical simulations. *Journal of Fluid Mechanics* **928**, A33.

GHODKE, C. D. & APTE, S. V. 2016 DNS study of particle-bed-turbulence interactions in an oscillatory wall-bounded flow. *Journal of Fluid Mechanics* **792**, 232–251.

GHODKE, C. D. & APTE, S. V. 2018 Roughness effects on the second-order turbulence statistics in oscillatory flows. *Computers & Fluids* **162**, 160–170.

GIBILARO, L. G., GALLUCCI, K., DI FELICE, R. & PAGLIAI, P. 2007 On the apparent viscosity of a fluidized bed. *Chemical Engineering Science* **62** (1), 294–300.

HAUSMANN, MAX, CHÉRON, VICTOR, EVRARD, FABIEN & VAN WACHEM, BEREND 2024 Study and derivation of closures in the volume-filtered framework for particle-laden flows. *Journal of Fluid Mechanics* **996**, A41.

HINO, M., SAWAMOTO, M. & TAKASU, S. 1976 Experiments on transition to turbulence in an oscillatory pipe flow. *Journal of Fluid Mechanics* **75** (2), 193–207.

HSU, TIAN-JIAN, JENKINS, JAMES T. & LIU, PHILIP L. F. 2004 On Two-Phase Sediment Transport: Sheet Flow of Massive Particles. *Proceedings: Mathematical, Physical and Engineering Sciences* **460** (2048), 2223–2250, arXiv: 4143214.

JENSEN, B. L., SUMER, B. M. & FREDSØE, J. 1989 Turbulent oscillatory boundary layers at high Reynolds numbers. *Journal of Fluid Mechanics* **206**, 265–297.

JEWEL, A., FUJISAWA, K. & MURAKAMI, A. 2019 Effect of seepage flow on incipient motion of sand particles in a bed subjected to surface flow. *Journal of Hydrology* **579**, 124178.

KASBAOUI, M. H. 2019 Turbulence modulation by settling inertial aerosols in Eulerian-Eulerian and Eulerian-Lagrangian simulations of homogeneously sheared turbulence. *Physical Review Fluids* **4** (12), 124308.

KASBAOUI, M. HOSSEIN & HERRMANN, MARCUS 2024 A High-Fidelity Methodology for Particle-Resolved Direct Numerical Simulations, arXiv: 2404.19030.

KASBAOUI, M. HOSSEIN, KOCH, DONALD L. & DESJARDINS, OLIVIER 2019 Clustering in Euler–Euler and Euler–Lagrange simulations of unbounded homogeneous particle-laden shear. *Journal of Fluid Mechanics* **859**, 174–203.

KEMPE, TOBIAS & FRÖHLICH, JOCHEN 2012 An improved immersed boundary method with direct forcing for the simulation of particle laden flows. *Journal of Computational Physics* **231** (9), 3663–3684.

KIDANEMARIAM, A. G. & UHLMANN, M. 2014 Interface-resolved direct numerical simulation of the erosion of a sediment bed sheared by laminar channel flow. *International Journal of Multiphase Flow* **67**, 174–188.

LIU, PHILIP L.-F., DAVIS, MATTHEW H. & DOWNING, SEAN 1996 Wave-induced boundary layer flows above and in a permeable bed. *Journal of Fluid Mechanics* **325**, 195–218.

MAXEY, MARTIN R. & RILEY, JAMES J. 1983 Equation of motion for a small rigid sphere in a nonuniform flow. *The Physics of Fluids* **26** (4), 883–889.

MAZZUOLI, M., BLONDEAUX, P., VITTORI, G., UHLMANN, M., SIMEONOV, J. & CALANTONI, J. 2020 Interface-resolved direct numerical simulations of sediment transport in a turbulent oscillatory boundary layer. *Journal of Fluid Mechanics* **885**.

MAZZUOLI, M., KIDANEMARIAM, A. G., BLONDEAUX, P., VITTORI, G. & UHLMANN, M. 2016 On the formation of sediment chains in an oscillatory boundary layer. *Journal of Fluid Mechanics* **789**, 461–480.

MAZZUOLI, MARCO, KIDANEMARIAM, AMAN G. & UHLMANN, MARKUS 2019 Direct numerical simulations of ripples in an oscillatory flow. *Journal of Fluid Mechanics* **863**, 572–600.

MAZZUOLI, M. & VITTORI, G. 2019 Turbulent spots in an oscillatory flow over a rough wall. *European Journal of Mechanics - B/Fluids* **78**, 161–168.

MEZA-VALLE, CLAUDIO & PUJARA, NIMISH 2022 Flow in oscillatory boundary layers over permeable beds. *Physics of Fluids* **34** (9), 092112.

O'DONOGHUE, TOM & WRIGHT, SCOTT 2004 Flow tunnel measurements of velocities and sand flux in oscillatory sheet flow for well-sorted and graded sands. *Coastal Engineering* **51** (11), 1163–1184.

OZDEMIR, C., HSU, T. J. & BALACHANDAR, S. 2014 Direct numerical simulations of transition and turbulence in smooth-walled Stokes boundary layer. *Physics of Fluids* **26**.

PEDOCCHI, F., CANTERO, M. I. & GARCÍA, M. H. 2011 Turbulent kinetic energy balance of an oscillatory boundary layer in the transition to the fully turbulent regime. *Journal of Turbulence* **12**, N32.

RAO, ARUN ASHOK & CAPECELATRO, JESSE 2019 Coarse-grained modeling of sheared granular beds. *International Journal of Multiphase Flow* **114**, 258–267.

SAFFMAN, P. G. 1965 The lift on a small sphere in a slow shear flow. *Journal of Fluid Mechanics* **22** (2), 385–400.

SALON, S., ARMENIO, V. & CRISE, A. 2007 A numerical investigation of the Stokes boundary layer in the turbulent regime. *Journal of Fluid Mechanics* **570**, 253–296.

SARPKAYA, T. 1993 Coherent structures in oscillatory boundary layers. *Journal of Fluid Mechanics* **253**, 105–140.

SCOTT, G. D. & KILGOUR, D. M. 1969 The density of random close packing of spheres. *Journal of Physics D: Applied Physics* **2** (6), 863–866.

SHUAI, SHUAI, DHAS, DARISH JESWIN, ROY, ANUBHAB & KASBAOUI, M. HOUSSSEM 2022 Instability of a dusty vortex. *Journal of Fluid Mechanics* **948**, A56.

SHUAI, SHUAI & KASBAOUI, M. HOUSSSEM 2022 Accelerated decay of a Lamb–Oseen vortex tube laden with inertial particles in Eulerian–Lagrangian simulations. *Journal of Fluid Mechanics* **936**.

SHUAI, SHUAI, ROY, ANUBHAB & KASBAOUI, M. HOUSSSEM 2024 The merger of co-rotating vortices in dusty flows. *Journal of Fluid Mechanics* **981**, A27.

SPARROW, KATHRYN, POKRAJAC, DUBRAVKA & VAN DER A, DOMINIC A. 2012 THE EFFECT OF BED PERMEABILITY ON OSCILLATORY BOUNDARY LAYER FLOW. *Coastal Engineering Proceedings* (33), 26–26.

STOKES, G. G. 1855 On the effects of internal friction of fluids on the motion of pendulums. *Transactions of the Cambridge Philosophical Society* **9**.

TENNETI, S., GARG, R. & SUBRAMANIAM, S. 2011 Drag law for monodisperse gas–solid systems using particle-resolved direct numerical simulation of flow past fixed assemblies of spheres. *International Journal of Multiphase Flow* **37** (9), 1072–1092.

UHLMANN, MARKUS 2005 An immersed boundary method with direct forcing for the simulation of particulate flows. *Journal of Computational Physics* **209** (2), 448–476.

VAN DOREN, JONATHAN S. & KASBAOUI, M. HOUSSSEM 2024 Turbulence modulation in dense liquid-solid channel flow. *Physical Review Fluids* **9** (6), 064306.

VITTORI, G., BLONDEAUX, P., MAZZUOLI, M., SIMEONOV, J. & CALANTONI, J. 2020 Sediment transport under oscillatory flows. *International Journal of Multiphase Flow* **133**, 103454.

VITTORI, G. & VERZICCO, R. 1998 Direct simulation of transition in an oscillatory boundary layer. *Journal of Fluid Mechanics* **371**, 207–232.

VOERMANS, J. J., GHISALBERTI, M. & IVEY, G. N. 2017 The variation of flow and turbulence across the sediment–water interface. *Journal of Fluid Mechanics* **824**, 413–437.

XIONG, CHENGWANG, QI, XIANG, GAO, ANKANG, XU, HUI, REN, CHENGJIAO & CHENG, LIANG
2020 The bypass transition mechanism of the Stokes boundary layer in the intermittently
turbulent regime. *Journal of Fluid Mechanics* **896**, A4.

YUAN, JING & MADSEN, OLE.S. 2014 Experimental study of turbulent oscillatory boundary
layers in an oscillating water tunnel. *Coastal Engineering* **89**, 63–84.